J. Fluid Mech. (2007), *vol.* 588, *pp.* 75–129.
doi:10.1017/S0022112007007409 Printed in the United Kingdom

Breakup of electrified jets

ROBERT T. COLLINS, MICHAEL T. HARRIS AND OSMAN A. BASARAN

Department of Chemical Engineering, Purdue University, West Lafayette, IN 47907, USA

(Received 12 May 2006 and in revised form 10 May 2007)

Breakup of electrified jets is important in applications as diverse as electrospraying, electroseparations and electrospray mass spectrometry. Breakup of a perfectly conducting, incompressible Newtonian liquid jet surrounded by a passive insulating gas that is stressed by a radial electric field is studied by a temporal analysis. An initially quiescent jet is subjected to axially periodic shape perturbations and the ensuing dynamics are followed numerically until pinch-off by both a three-dimensional but axisymmetric (two-dimensional) and a one-dimensional slender-jet algorithm. Results computed with these algorithms are verified against predictions from linear theory for short times. Breakup times, ratios of the sizes of the primary to satellite drops formed at pinch-off, and the Coulombic stability of these drops are reported over a wide range of electrical Bond numbers, N_E (ratio of electric to surface tension force), Ohnesorge numbers, N_{Oh} (ratio of viscous to surface tension force), and disturbance wavenumbers, k. Effect of surface charge on interface overturning is investigated. Furthermore, the influence of electrostatic stresses on the dynamics of pinch-off and the mechanisms of satellite drop formation is also addressed.

1. Introduction

The formation of drops of a liquid that is flowing out of a nozzle by dripping or jetting in the absence or presence of electric fields is of immense scientific and technological importance (Eggers 1997; Basaran 2002). A number of fascinating electrohydrodynamic (EHD) flow transitions are known to occur as the flow rate of the liquid in the nozzle and/or the strength of the electric field that the drop is being subjected to are varied, as shown schematically in figure 1 (Cloupeau & Prunet-Foch 1989, 1990; Zhang & Basaran 1996). Over certain regions of the parameter space governing the problem, the interface separating the drop from the ambient fluid is nearly conical in shape and a fine jet issues from the tip of the drop (Zeleny 1917; Taylor 1964, 1969; Hayati, Bailey & Tadros 1987*a*, *b*). The latter mode of EHD jetting is now called the cone-jet mode of atomization (Cloupeau & Prunet-Foch 1989). Cone-jetting and some of the other phenomena depicted in figure 1 whereby fine electrified jets form and sometimes subsequently break into drops are widely used in applications as diverse as spraying (Vonnegut & Neubauer 1952; Jones & Thong 1971), fibre spinning (Doshi & Reneker 1995; Reneker *et al.* 2000; Yarin, Koobhongse & Reneker 2001; Hohman *et al.* 2001*a, b*), synthesis of ceramic particles (Harris, Scott & Byers 1993), mass spectrometry (Cook 1986; Fenn *et al.* 1990), and ink-jet printing (Sweet 1965). Although complete theoretical understanding of drop and jet breakup in the presence of electric fields is challenging and requires a number of different approaches that depend on the specific situation under consideration (Gañan-Cálvo 1997; Cherney 1999; Higuera 2004; Notz & Basaran 1999; Reznik

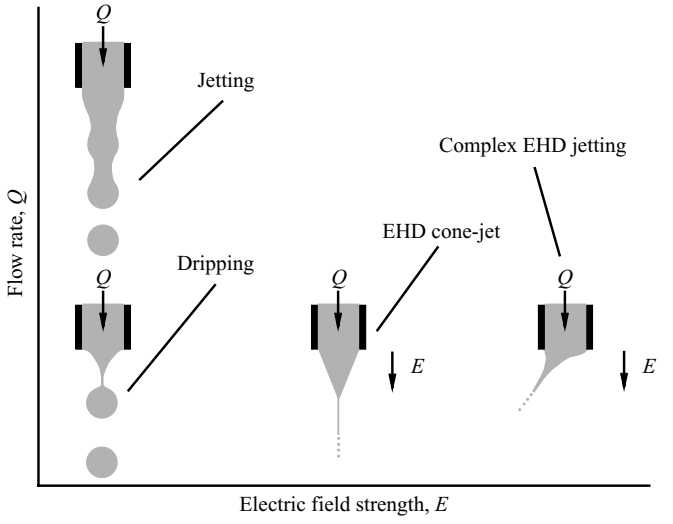

FIGURE 1. Phase diagram depicting flow transitions that occur as flow rate and/or electric field strength are varied.

et al. 2004), a problem that is of central importance in the field is the capillary pinching of filaments that are subjected to an electric field. The major goal of this paper is to advance the state of understanding of capillary pinching and breakup of such filaments through the use of high-accuracy computation.

The stability and breakup of uncharged liquid jets have been studied extensively, beginning with the pioneering works of Plateau (1863) and Rayleigh (1879), who demonstrated that a liquid filament is unstable to axisymmetric disturbances for which the wavelength of the disturbance exceeds the circumference of the filament. Lord Rayleigh's linear analysis showed that, when the fluid viscosity is negligible, the fastest growing axisymmetric disturbances correspond to an axial wavenumber $\tilde{k}_{max} \approx 0.7/\tilde{R}$, where $\tilde{R}$ is the radius of the unperturbed filament, and that non-axisymmetric disturbances are stable. Rayleigh (1892) later examined the linear stability of highly viscous or Stokes jets, showing that the fastest growing disturbances correspond to the long-wave limit. Basset (1894), Chandrasekhar (1961) and others extended Rayleigh's analysis, providing temporal analyses of the linear stability of Newtonian liquid jets of arbitrary viscosity to infinitesimal-amplitude axisymmetric disturbances. Goedde & Yuen (1970) carried out a series of experiments with harmonically forced jets and showed that observed growth rates compare favourably with linear theory. While linear stability analyses such as these provide useful estimates of disturbance growth rates and the sizes of the drops formed at breakup, other essential features of jet breakup, such as the formation of satellite drops interspersed between the large primary drops, cannot be predicted by these techniques. Later authors (Yuen 1968; Nayfeh 1970; Lafrance 1975; Chaudhary & Redekopp 1980) examined the nonlinear deformation of uncharged jets through higher-order perturbation analyses, which associate the development of satellite drops with the growth of higher harmonics. Yuen's analysis, as demonstrated by Chaudhary & Redekopp, predicts the formation of satellite drops at all unstable wavenumbers. A number of authors have examined the dynamics of the breakup of uncharged jets using one-dimensional approximations of the equations of motion (Lee 1974; Yarin 1993; Eggers & Dupont 1994; Papageorgiou 1995). Computational analyses of the deformation and breakup

of uncharged jets which solve the full three-dimensional but axisymmetric or two-dimensional equations of motion (Laplace, Stokes and Navier–Stokes) have also been reported. Mansour & Lundgren (1990) examined the formation of satellite drops computationally, using a boundary-element algorithm to perform a temporal analysis of jet breakup in the inviscid limit, demonstrating reasonably good agreement with the experimental studies of satellite drop formation by Rutland & Jameson (1970). Ashgriz & Mashayek (1995) used a Galerkin finite-element algorithm to study the deformation and breakup of Newtonian jets of arbitrary viscosity, demonstrating excellent agreement with Chandrasekhar's linear theory at small times and with Rutland & Jameson's experimental analysis of drop sizes.

A number of workers have examined the stability of liquid jets stressed by radial electric fields through linear analysis. The first such analysis was performed by Basset (1894), who extended Rayleigh's (1879) analysis to investigate the stability of perfectly conducting jets to axisymmetric disturbances. Basset's analysis shows that electrostatic stresses are stabilizing for long waves and destabilizing for short waves, with the transition occurring at wavenumber $\tilde{k}_E \approx 0.6/\tilde{R}$. Errors in Basset's analysis were later corrected by Taylor (1969). Melcher (1963) and Huebner & Chu (1971) extended this analysis for inviscid jets to include both axisymmetric and non-axisymmetric disturbances. Saville (1971) examined the stability of perfectly conducting Newtonian jets of arbitrary viscosity stressed by radial electric fields to infinitesimal amplitude axisymmetric and non-axisymmetric disturbances, showing that electrostatic stresses in this configuration tend to destabilize the non-axisymmetric modes. For highly viscous jets, viscous damping of axisymmetric disturbances leads to a situation where the sinuous mode becomes the most unstable (Saville 1971; Cloupeau & Prunet-Foch 1989; Yarin, Kataphinan & Reneker 2005). This phenomenon is observed experimentally as so-called kink instabilities. López-Herrera, Riesco-Chueca & Gañan-Cálvo (2005) performed a linear stability analysis of the problem for imperfectly conducting liquid jets based on the Taylor–Melcher leaky-dielectric model (Melcher & Taylor 1969; Saville 1997).

There have been few studies of the nonlinear dynamics and breakup of liquid jets stressed by radial electric fields. Setiawan & Heister (1997) performed a temporal analysis of the axisymmetric breakup of a perfectly conducting liquid jet stressed by a radial electric field in the inviscid limit, using a three-dimensional but axisymmetric boundary-element algorithm similar to that used by Mansour & Lundgren (1990). These authors prescribed the value of the electric potential on the surface of their jet and considered primarily breakup at very high electric field strengths, reporting results for jet breakup times and for the sizes of the primary and satellite drops formed at pinch-off. While these authors show favourable agreement between the results of their algorithm at small times with Melcher's linear theory, a number of the results reported in that work appear to be mesh dependent. López-Herrera, Gañan-Cálvo & Perez-Saborid (1999) studied axisymmetric jet breakup for perfectly conducting Newtonian jets stressed by radial electric fields using a one-dimensional algorithm based on the viscous Lee model (Lee 1974). In contrast to Setiawan & Heister, these authors prescribed the value of the surface charge carried by their jets. López-Herrera *et al*.'s analysis is restricted to low to moderate viscosities and electric field strengths, as these are the conditions for which axisymmetric disturbances grow much faster than non-axisymmetric ones (Melcher 1963; Saville 1971; Yarin *et al.* 2005). These authors report, among other things, the electric field strength, viscosity and disturbance wavenumber dependence of jet breakup times and the sizes and charges of the drops formed at pinch-off. López-Herrera & Gañan-Cálvo (2004)

later compared the predictions of this one-dimensional algorithm with experiments, approximating an axisymmetric electric field by using widely spaced parallel-plate electrodes. Their interest was primarily concerned with influence of viscosity and electric field strength on the distribution of volume and charge between the primary and satellite drops formed at pinch-off. These authors observed reasonably good agreement between the predictions of their algorithm and experiments, particularly at low to moderate electric field strengths. López-Herrera & Gañan-Cálvo reported results over a narrow range of the dimensionless ratio of the viscous to surface tension force or the Ohnesorge number, N_{Oh}, in that $0.079 \leqslant N_{Oh} \leqslant 0.271$.

One-dimensional models such as the viscous Lee model and others based on the so-called slender-jet equations (Eggers 1993; Yarin 1993; Papageorgiou 1995) have been shown to be highly accurate in predicting the gross phenomena associated with capillary breakup, including breakup times and the sizes of the drops formed at pinch-off. However, direct comparison with more robust and accurate techniques which solve the full three-dimensional but axisymmetric or two-dimensional equations of motion reveal that, while these one-dimensional algorithms can be very accurate, their accuracy is usually limited to some portion of the parameter space of the problem at hand (Yildirim & Basaran 2001; Ambravaneswaran, Wilkes & Basaran 2002).

The goal of this work is to examine computationally through a temporal analysis the axisymmetric deformation and breakup of perfectly conducting, Newtonian jets of arbitrary viscosity stressed by the application of a radial electric field. Section 2 presents the governing equations, and boundary and initial conditions, and details the numerical methods used. This section describes a robust and accurate Galerkin finite-element algorithm that has been developed to solve the three-dimensional but axisymmetric Navier–Stokes system and Laplace's equation. This algorithm is similar to the algorithms used in Chen, Notz & Basaran (2002) and Notz & Basaran (2004), which have been shown to be extremely accurate at tracking capillary breakup all the way to pinch-off. Both Setiawan & Heister (1997) and López-Herrera & Gañan-Cálvo (2004) in their studies of charged inviscid and moderately viscous jets, respectively, have continued their calculations until the dimensionless minimum radius of the jet is about 0.01. Chen *et al.* (2002), among others, have shown that one must typically continue calculations until the neck radius is about an order of magnitude smaller than this value to gain insights into the local dynamics at the incipience of breakup and to capture fully the formation of satellites. Additionally, this section describes a hybrid Galerkin finite-element algorithm that has been developed which couples a one-dimensional slender-jet description of the equations of motion with a three-dimensional but axisymmetric representation of the electric field external to the jet. Section 3 presents computational results and gives a detailed comparison of the algorithms used. Breakup times and the sizes and charges of the drops formed at pinch-off are reported for a wide range of wavenumbers, viscosities and electric field strengths. The mechanisms for satellite formation in charged jets are discussed in detail, and the Coulombic stability of the drops formed at pinch-off is examined. A discussion of the dynamics of pinch-off is also given. Concluding remarks are presented in § 4.

2. Mathematical formulation and numerical analysis

The system of interest (figure 2) consists of an axisymmetric perfectly conducting liquid filament surrounded by an insulating gas of permittivity ϵ that is in turn

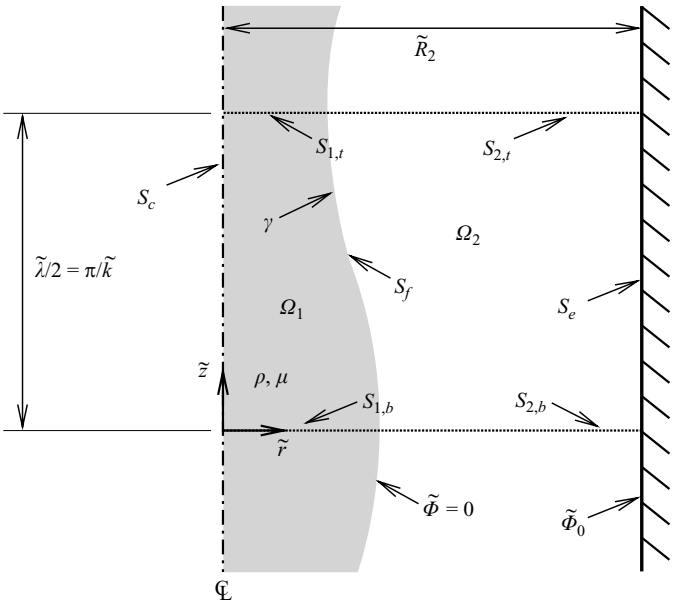

FIGURE 2. Definition sketch.

bounded by a concentric cylindrical electrode of radius $\tilde{R}_2$. The liquid comprising the filament is an incompressible, Newtonian fluid of constant and spatially uniform density ρ and viscosity μ. The gas enveloping the filament is dynamically inactive and exerts a constant pressure, which is taken as the datum level of pressure, on the filament. The surface tension γ of the liquid–gas interface is constant and spatially uniform. Both the electrode and the jet are equipotentials, and the potential difference between them is $\tilde{\Phi}_0$ for all times $\tilde{t}$. For the temporal analyses of electrocapillary jet breakup that are of interest in this work, the frame of reference travels with the filament. In this frame, the filament is quiescent and has a uniform radius $\tilde{R}_1$ for times $\tilde{t} < 0$. At time $\tilde{t} = 0$, the free surface of the filament is subjected to an axially periodic perturbation of magnitude $\tilde{\varepsilon}$ and axial wavenumber $\tilde{k}$ (or wavelength $\tilde{\lambda}$, with $\tilde{\lambda} = 2\pi/\tilde{k}$), generating an electrocapillary pressure gradient along the jet which drives fluid flow for times $\tilde{t} > 0$.

For mathematical convenience, a cylindrical coordinate system $(\tilde{r}, \theta, \tilde{z})$ is employed with the common axis of the filament and the electrode coinciding with the $\tilde{z}$-direction. The formulation is independent of the meridional angle θ as only axisymmetric configurations are considered. The portion of the physical domain of interest occupied by the filament at time $\tilde{t}$ is denoted Ω_1, and the remainder, comprised of the surrounding gas, is denoted Ω_2. S_f, S_c and S_e, then, denote the liquid–gas interface, the centreline of the filament, and the inner surface of the electrode, respectively. Owing to symmetry, the physical domain can be restricted axially to half a wavelength, $\tilde{\lambda}/2$. The upper and lower boundaries of Ω_1 (Ω_2), denoted $S_{1,t}$ ($S_{2,t}$) and $S_{1,b}$ ($S_{2,b}$), respectively, are then defined such that $S_{1,t}$ ($S_{2,t}$) is located at the neck (i.e. the narrowest point) and $S_{1,b}$ ($S_{2,b}$) is located at the swell (i.e. the widest point) of the initial perturbation of the free surface, with $\tilde{z} = 0$ corresponding to the axial location of $S_{1,b}(S_{2,b})$.

Throughout this paper, for consistency of nomenclature, variables appearing with a tilde over them are the dimensional analogues of variables that appear without a tilde. For succinctness, the governing equations, initial conditions (ICs), boundary

conditions (BCs) and results are presented hereinafter in dimensionless form. The characteristic length, time and electric potential are, respectively, the unperturbed filament radius $\tilde{R}_1$, capillary time scale $t_c \equiv \sqrt{\rho \tilde{R}_1^3/\gamma}$, and potential difference between the electrode and the jet $\tilde{\Phi}_0$. The characteristic scale for surface charge density is $\gamma/\tilde{\Phi}_0$. The dimensionless groups governing the dynamics of the system are the Ohnesorge number $N_{Oh} \equiv \sqrt{\mu^2/\gamma\rho\tilde{R}_1}$, which compares the relative importance of viscous forces to capillary forces, the electric Bond number $N_E \equiv \epsilon\tilde{\Phi}_0^2/2\gamma\tilde{R}_1$, which compares the relative importance of electrostatic forces to capillary forces, the wavenumber $k = \tilde{R}_1\tilde{k}$, the electrode radius $R = \tilde{R}_2/\tilde{R}_1$, and the perturbation amplitude $\varepsilon = \tilde{\varepsilon}/\tilde{R}_1$. Though not necessary, it will be advantageous later to define an additional dimensionless group, $N_E' \equiv 2N_E/\log^2(R)$. A brief explanation of the choice of parameter values examined in this work and of the appropriateness of the perfect-conductor model is given in Appendix A.

The dynamics of the filament are governed by the Navier–Stokes system,

$$\nabla\cdot\boldsymbol{v} = 0, \tag{2.1}$$

$$\frac{\partial \boldsymbol{v}}{\partial t} + \boldsymbol{v}\cdot\nabla\boldsymbol{v} - N_{Oh}\,\nabla\cdot\boldsymbol{T} = \boldsymbol{0}, \tag{2.2}$$

where $\boldsymbol{v}$ is the velocity vector and $\boldsymbol{T}$ is the stress tensor, $\boldsymbol{T} = -p\boldsymbol{I} + (\nabla\boldsymbol{v} + (\nabla\boldsymbol{v})^T)$, which is measured in units of μ/t_c. The electric field $\boldsymbol{E}$ in the gas surrounding the filament is given by the negative gradient of the scalar potential Φ and is necessarily zero in the perfectly conducting filament. The electric potential is governed by Laplace's equation:

$$\nabla^2\Phi = 0. \tag{2.3}$$

Equations (2.1) and (2.2) in Ω_1 and (2.3) in Ω_2 are solved subject to the kinematic (2.4) and traction (2.5) BCs along the free surface S_f:

$$\boldsymbol{n}\cdot(\boldsymbol{v} - \boldsymbol{v}_s) = 0, \tag{2.4}$$

$$\boldsymbol{n}\cdot[\boldsymbol{T}] - N_{Oh}^{-1}(-2\mathscr{H})\,\boldsymbol{n} = \boldsymbol{0}, \tag{2.5}$$

where $-2\mathscr{H} = \nabla_S\cdot\boldsymbol{n}$ is twice the local mean curvature, $\boldsymbol{n}$ is the outward pointing unit normal to S_f, and $\boldsymbol{v}_s$ is the local velocity of S_f. Equation (2.4) requires that there be no mass flux across S_f, while (2.5) equates the jump in the local stress vector across the free surface to the local capillary pressure. Here, the jump in the local stress vector is $\boldsymbol{n}\cdot[\boldsymbol{T}] = \boldsymbol{n}\cdot(\boldsymbol{T}_E - \boldsymbol{T})$, where $\boldsymbol{T}_E$ is the electrostatic Maxwell stress tensor (Melcher & Taylor 1969),

$$\boldsymbol{T}_E = N_E(2\boldsymbol{E}\boldsymbol{E} - E^2\boldsymbol{I}). \tag{2.6}$$

Because of the periodic nature of the initial disturbance, the shear stress and axial component of the velocity $v = \boldsymbol{e}_z\cdot\boldsymbol{v}$ vanish along $S_{1,b}$ and $S_{1,t}$,

$$\boldsymbol{e}_r\boldsymbol{e}_z : \boldsymbol{T} = 0, \tag{2.7}$$

$$v = 0, \tag{2.8}$$

where $\boldsymbol{e}_r$ and $\boldsymbol{e}_z$ are the radial and axial unit vectors, and the axial component of the electric field in the gas surrounding the filament likewise vanishes along $S_{2,b}$ and $S_{2,t}$,

$$\boldsymbol{e}_z\cdot\boldsymbol{E} = -\boldsymbol{e}_z\cdot\nabla\Phi = 0. \tag{2.9}$$

Similarly, because of axisymmetry, the shear stress and the radial component of the velocity $u = \boldsymbol{e}_r \cdot \boldsymbol{v}$ vanish along the centreline of the filament S_c:

$$\boldsymbol{e}_z \boldsymbol{e}_r : \boldsymbol{T} = 0, \tag{2.10}$$

$$u = 0. \tag{2.11}$$

The Dirichlet conditions on the electric potential described above are

$$\Phi = 0 \tag{2.12}$$

along S_f, and

$$\Phi = 1 \tag{2.13}$$

along S_e.

In this work, the breakup of electrified jets in the Stokes flow limit is also examined. Here, the appropriate time scale is $\mu \tilde{R}_1/\gamma$, rather than the capillary time scale t_c used in the Newtonian case. The characteristic length and electric potential scales used for Newtonian jets ($\tilde{R}_1$ and $\tilde{\Phi}_0$) are retained. The dimensionless Navier–Stokes equation, (2.2), is replaced with the dimensionless Stokes equation,

$$\nabla \cdot \boldsymbol{T} = \boldsymbol{0}, \tag{2.14}$$

where $\boldsymbol{T}$ is measured in units of $\gamma/\tilde{R}_1$, and the traction BC, (2.5), is modified to reflect the change of scales:

$$\boldsymbol{n} \cdot [\boldsymbol{T}] - (-2\mathscr{H})\,\boldsymbol{n} = \boldsymbol{0}. \tag{2.15}$$

The dimensionless forms of the remaining governing equations and BCs are the same as those used in the Newtonian case. In the Stokes limit, N_{Oh} is eliminated as a parameter.

2.1. *Development of the two-dimensional algorithm*

In this subsection, an algorithm is developed to solve the full three-dimensional but axisymmetric problem described above, which is hereinafter referred to as the two-dimensional algorithm. The system of spatially two-dimensional partial differential equations (PDEs) described by (2.1), (2.2) and (2.3) and BCs described by (2.4)–(2.13) are solved by a method of lines, with the Galerkin/finite-element method (G/FEM) (Strang & Fix 1973) for spatial discretization and an adaptive finite-difference technique for time integration (Gresho, Lee & Sani 1980). Mixed interpolation (Huyakorn *et al.* 1978) is used in expanding $\boldsymbol{v}$, p and Φ, where bilinear basis functions are used for expanding p and biquadratic basis functions are used for expanding $\boldsymbol{v}$ and Φ. The physical domain is subdivided into a set of smaller sub-domains, or elements. Each element in the physical domain (r, z) is isoparametrically mapped to a unit square in the computational domain (ξ, η).

The presence of a deforming free surface requires that the mesh used to tessellate the spatial domain be able to move and deform. To accomplish this, a new adaptive tessellation method that combines desirable features of both elliptic and algebraic mesh generation, as described in Appendix B.1, is used. The elliptic mesh generation algorithm used is based on the method of Christodoulou & Scriven (1992). Here, a weighted combination of functionals imposing smoothness of coordinate lines, functionals imposing orthogonality of coordinate lines, and regularization terms allowing for controlled distribution of elements is constructed and employed to determine the locations of the N mesh points (r_i, z_i), $i = 1, \ldots, N$. The resulting set of PDEs is cast as Galerkin weighted residuals, with (r_i, z_i) expanded in biquadratic

basis functions. These weighted residuals are solved simultaneously with the weighted residuals of the physical equations.

The spatial discretization of the problem by G/FEM results in a system of nonlinear differential and algebraic equations (DAEs). This system is integrated in time using a predictor–corrector method, with time derivatives at each time step approximated by either a first-order backward difference or a second-order trapezoid rule. To smooth unphysical transients that arise from the application of inconsistent ICs, eight backward difference steps are used initially (Luskin & Rannacher 1982; Brenan, Campbell & Petzold 1996). Subsequent time steps use the trapezoid rule, with the step size determined adaptively. A first-order forward difference predictor is used with the backward difference corrector, and a second-order Adams–Bashforth predictor is used with the trapezoid rule corrector.

After spatial and temporal discretization of the problem, the resulting system of algebraic equations is solved iteratively using a fully coupled Newton's method with an analytically computed Jacobian. The correctness of the Jacobian is demonstrated by the quadratic convergence of Newton's method. A frontal solver based on the algorithm of Hood (1976) is used to solve the system of algebraic equations for each Newton iteration. Newton iterations are continued until the L_2 norm of both the residuals and updates falls below 10^{-6}. Typically, this requires two to four Newton iterations per time step. Computations are continued until the minimum jet radius h_{min} reaches 2×10^{-3}.

In addition to mesh refinement, described in Appendix B.1, a number of tests are performed to determine the correctness and accuracy of the two-dimensional algorithm. For each simulation, the computed jet volume V is found to vary by less than 0.05% over the course of the computation. Additionally, for uncharged jets ($N_E = 0$), computed results obtained using the two-dimensional algorithm, including breakup times and the sizes of the drops formed at pinch-off, are found to be in excellent agreement with results reported by Ashgriz & Mashayek (1995). Further, computational results are compared with linear theory, as described in § 3.1. A comparison of computed results with previous works involving electrified jets is given in subsequent sections.

2.2. *Development of the one-dimensional algorithm*

In this subsection, a hybrid algorithm, which is hereinafter referred to as the one-dimensional algorithm, is developed to solve simultaneously the full three-dimensional but axisymmetric Laplace equation in Ω_2 coupled with a slender-jet representation of the Navier–Stokes system in Ω_1. Following Yarin (1993), Eggers & Dupont (1994) and Papageorgiou (1995), the spatially two-dimensional Navier–Stokes system in Ω_1 is reduced to a spatially one-dimensional system of PDEs. This spatially one-dimensional theory keeps only the leading-order terms in Taylor series expansions in the radial coordinate of the axial velocity v and pressure p, but retains in full the curvature and Maxwell stress terms in the traction BC. Previous studies (Eggers 1993, 2005; Yarin 1993; Eggers & Dupont 1994; Zhang, Padgett & Basaran 1996; Ambravaneswaran & Basaran 1999; Yildirim & Basaran 2001; Ambravaneswaran *et al.* 2002) justify retention of the full curvature term, as its retention has been shown to yield a superior description of nonlinear interface shape evolution than can be obtained with the truncated curvature required for proper slender-jet asymptotics. Both López-Herrera *et al.* (1999) and López-Herrera & Gañan-Cálvo (2004) retain the full Maxwell stress in their analyses of charged jet breakup.

The resulting set of one-dimensional equations governing $v \equiv v(z,t)$ and $h \equiv h(z,t)$, where $r = h(z,t)$ is the free surface location, are

$$\frac{\partial h}{\partial t} + v\frac{\partial h}{\partial z} + \frac{1}{2}\frac{\partial v}{\partial z}h = 0, \tag{2.16}$$

$$\frac{\partial v}{\partial t} + v\frac{\partial v}{\partial z} + N_{Oh}\frac{\partial \mathscr{P}}{\partial z} - 3N_{Oh}\frac{1}{h^2}\frac{\partial}{\partial z}\left(h^2\frac{\partial v}{\partial z}\right) = 0. \tag{2.17}$$

Here, $\mathscr{P}$ is the electrocapillary pressure, i.e. the sum of capillary and electrical pressures,

$$\begin{aligned}\mathscr{P} &= \frac{-2\mathscr{H}}{N_{Oh}} - \frac{1}{N_{Oh}}(\boldsymbol{n}\cdot\boldsymbol{T}_E\cdot\boldsymbol{n}) \\ &= \frac{1}{N_{Oh}}\left[\frac{1}{h(1+(\partial h/\partial z)^2)^{1/2}} - \frac{\partial^2 h/\partial z^2}{(1+(\partial h/\partial z)^2)^{3/2}}\right] - \frac{N_E}{N_{Oh}}\left[\left(\frac{\partial \Phi}{\partial r}\right)^2 + \left(\frac{\partial \Phi}{\partial z}\right)^2\right]\end{aligned} \tag{2.18}$$

and pressure p in the bridge, to the leading-order, is $p = \mathscr{P} - N_{Oh}\partial v/\partial z$. In slender-jet theory, the radial velocity is simply $u = -(r/2)\partial v/\partial z$. Boundary conditions to complete the system of PDEs require that $\partial h/\partial z = 0$ and $v = 0$ at the upper and lower boundaries of the one-dimensional domain, i.e. $z = 0$, $z = \pi/k$.

As with the two-dimensional algorithm, the system of PDEs described by (2.3), (2.16) and (2.17) is solved by a method of lines, with G/FEM for spatial discretization and adaptive finite differences for time integration. The unknowns h and v, and an additional auxiliary unknown $\Omega \equiv \partial h/\partial z$ (Zhang *et al.* 1996), are expanded using a set of quadratic basis functions. The one-dimensional domain, $0 \leqslant z \leqslant \pi/k$, is divided into a series of elements, and each element in the physical domain (z) is isoparametrically mapped to a unit line segment in the computational domain (ξ).

Solution of Laplace's equation in Ω_2 is accomplished in a manner analogous to that described in § 2.1. As with the two-dimensional algorithm, an adaptive mesh is required to tessellate Ω_2 owing to the presence of the free surface, S_f. For the one-dimensional algorithm, the method of spines (Kistler & Scriven 1994; Wilkes, Phillips & Basaran 1999) is used to determine the location of the N mesh points in Ω_2. Here, spines of constant z, which are uniformly distributed along the length of the jet, correspond to the η coordinate lines (S_f is a ξ coordinate line), and a weighting function is applied to concentrate the ξ coordinate lines near S_f. This technique is prone to failure when S_f becomes very deformed, i.e. when the magnitude of $\partial h/\partial z$ becomes very large or when the shape function h is not a single-valued function of z. However, the same drawback is inherent in the slender-jet description of the dynamics, which requires that h be a single-valued function of z, so that the use of constant z spines poses no additional drawbacks. Further, this technique is computationally less expensive than elliptic mesh generation used in the two-dimensional algorithm, as the mesh point locations are not solved for independently, but are instead determined along each spine from the free-surface coordinate h and the prescribed weighting function.

After spatial discretization of the problem is accomplished, temporal discretization of the resulting system of nonlinear DAEs is performed. The same time integration algorithm used in the two-dimensional algorithm is used in the one-dimensional algorithm. After spatial and temporal discretization, the resulting system of nonlinear algebraic equations is solved iteratively using a fully coupled Newton's method with an analytically computed Jacobian. A new arrow solver, similar to that developed

earlier by Thomas & Brown (1987), is used to solve the system of algebraic equations at each Newton iteration. The criteria used for judging convergence of Newton's method and deciding when breakup has occurred follow those already described in the previous subsection.

Mesh refinement for the one-dimensional algorithm is described in Appendix B.2. Tests used to determine the correctness and accuracy of the one-dimensional algorithm are similar to those used with the two-dimensional algorithm. For each computation performed, the total jet volume V varies by less than 0.5% from its initial value. Comparisons of computed results with linear theory and an extensive comparison of computed results from the two- and one-dimensional algorithms are given in subsequent sections.

The slender-jet algorithms developed by López-Herrera *et al.* (1999) and López-Herrera & Gañan-Cálvo (2004) do not prescribe a fixed electric potential for the jet, as is done here, but instead impose that the total surface charge carried by the jet is temporally constant; the electric potential of the jet (which is modelled as a perfect conductor and hence as an equipotential) is computed at each time step to satisfy this constraint. A direct comparison of results obtained with the one-dimensional algorithm to those reported in these works, therefore, is inappropriate, as the problems being investigated are physically different.

3. Results and discussion

3.1. *Comparison of the one- and two-dimensional algorithms with linear theory*

Although linear stability analysis is incapable of predicting a number of important features of jet breakup, e.g. the formation of satellite droplets, it is an invaluable tool because it provides information about regions of the parameter space for which a liquid filament is stable or unstable and yields the growth rate of disturbances. Previous works with uncharged filaments have shown that growth rates obtained both experimentally (Goedde & Yuen 1970) and computationally (Ashgriz & Mashayek 1995) agree strikingly well with linear theory, with agreement breaking down only in the early and final stages of breakup (see below). As a consequence, linear theory can provide reasonable estimates of breakup times. These facts are exploited in this work for the purposes of code validation and developing intuition into the underlying physics which is essential for understanding the nonlinear results. Growth rates and breakup times obtained from simulations using the one- and two-dimensional algorithms are compared below with linear theory.

The appropriate dispersion relation for this analysis is a slight modification of a result due to Saville (1971), who examined the linear stability of a perfectly conducting Newtonian liquid jet stressed by a radial electric field to an infinitesimal amplitude surface disturbance that is proportional to $\exp[\omega t + \mathrm{i}kz]$, where ω is the growth rate of the disturbance. Saville places the electrode at infinity, in effect eliminating R as a parameter. When cast in terms of the dimensionless groups used in this work, Saville's dispersion relation, when only axisymmetric motions are considered, is

$$\frac{\Omega(k, R, N_E)}{N_{Oh}^2} k \frac{I_1(k)}{I_0(k)} = (\beta^4 - k^4) + 2k \left(\frac{kI_0(k) - I_1(k)}{I_0(k)} \right) \times \left[(\beta^2 + k^2) - 2k^2 \frac{I_1(k)}{I_1(\beta)} \left(\frac{\beta I_0(\beta) - I_1(\beta)}{kI_0(k) - I_1(k)} \right) \right] \tag{3.1}$$

with

$$\Omega = 1 - k^2 - \frac{2N_E}{\log^2(R)}\left(1 - k\frac{K_1(k)}{K_0(k)}\right). \tag{3.2}$$

Here, I_n and K_n denote modified Bessel functions of the first and second kind of order n, respectively, and $\beta^2 \equiv k^2 + \omega/N_{Oh}$. The presence of a term involving R in (3.2) stems from differences in the characteristic scales used in the two formulations. Instead of using the potential difference $\tilde{\Phi}_0$ as a characteristic scale for the electric potential, Saville uses the electric field at the free surface of the (unperturbed) jet $\tilde{E}_0$. This leads to a different definition of the electric Bond number in Saville's formulation, $N'_E \equiv \varepsilon \tilde{R}_1 \tilde{E}_0^2/\gamma$. It is trivial to show that $\tilde{E}_0 = -\tilde{\Phi}_0/(\tilde{R}_1 \ln(\tilde{R}_2/\tilde{R}_1))$, whence $N'_E = 2N_E/\log^2(R)$.

The quantity Ω defined by (3.2) is proportional to the difference in electrocapillary pressure (i.e. $p_C + p_E$, where $p_C \equiv -2\mathscr{H}/N_{Oh}$ and $p_E \equiv (-\boldsymbol{n}\cdot\boldsymbol{T}_E\cdot\boldsymbol{n})/N_{Oh}$) between the neck and the swell and hence may be interpreted as the electrocapillary driving force for flow from the neck to the swell. The sign of Ω determines the stability of the jet to the applied surface disturbance: a jet will be unstable (stable) to a surface disturbance for which $\Omega > 0\,(\Omega < 0)$. It is worth noting here that there exists a wavenumber k_E such that $k_E K_1(k_E)/K_0(k_E) = 1$ ($k_E \approx 0.595$) for which the electrostatic contribution to Ω vanishes and the linear growth rate of the surface disturbance is independent of N_E.

To account properly for a finite R requires that (3.2) be modified as follows:

$$\Omega = 1 - k^2 - N'_E\left(1 + k\frac{I_1(k)K_0(kR) + I_0(kR)K_1(k)}{I_0(k)K_0(kR) - I_0(kR)K_0(k)}\right). \tag{3.3}$$

Equations (3.1) and (3.3) reduce in the inviscid limit to Melcher's (1963) dispersion relation. Saville's dispersion relation is recovered in the limit as $R \to \infty\,(R >> 1/k)$ holding N'_E constant. For the modified dispersion relation, $k_E = k_E(R)$ with $k_E(R) \to 0.595$ in the limit as $R \to \infty\,(R >> 1/k)$. Also, when $N'_E = 0$, equations (3.1) and (3.3) reduce to Chandrasekhar's (1961) dispersion relation for an uncharged filament.

The influence of electrostatic stresses on jet stability can be elucidated by examining two limiting forms of (3.3). In the long-wave limit ($k \to 0$), for which capillary stresses are destabilizing, $\Omega \to 1 - N'_E[1 - 1/\log(R)]$. In this limit, for sufficiently large R, electrostatic stresses are stabilizing, acting either to mitigate the influence of capillary stresses or, for sufficiently large N'_E, to reverse the direction of the driving force entirely, rendering the jet stable. In the short-wave limit ($k \to \infty$), for which capillary stresses are stabilizing, $\Omega \to -k^2 + N'_E[k\coth(k(R-1))]$, or, for $R - 1 >> 1/k$, $\Omega \to -k^2 + N'_E k$. Here, as opposed to the long-wave limit, electrostatic stresses are destabilizing. In light of these limiting cases, several prominent features of the dispersion relation described by (3.1) and (3.3) become apparent, the most obvious being the existence of a wavenumber k_E demarcating the transition from stabilizing electrostatic stresses in the long-wave limit to destabilizing electrostatic stresses in the short-wave limit. Other features of the dispersion relation are best viewed in relation to Chandrasekhar's result for an uncharged filament, where the range of unstable disturbance wavenumbers is $0 \leqslant k < k_{crit}$, with the upper cutoff wavenumber for stability $k_{crit} = 1$. For a charged filament, k_{crit} increases with increasing N'_E owing to the destabilizing influence of electrostatic stresses for $k > k_E$. Additionally, for sufficiently large N'_E, the stabilizing influence of electrostatic stresses in the long-wave limit leads to the development of a stable region $0 \leqslant k < k'_{crit}$, so that the range of unstable wavenumbers becomes $k'_{crit} < k < k_{crit}$. The wavenumber k_{max} associated with

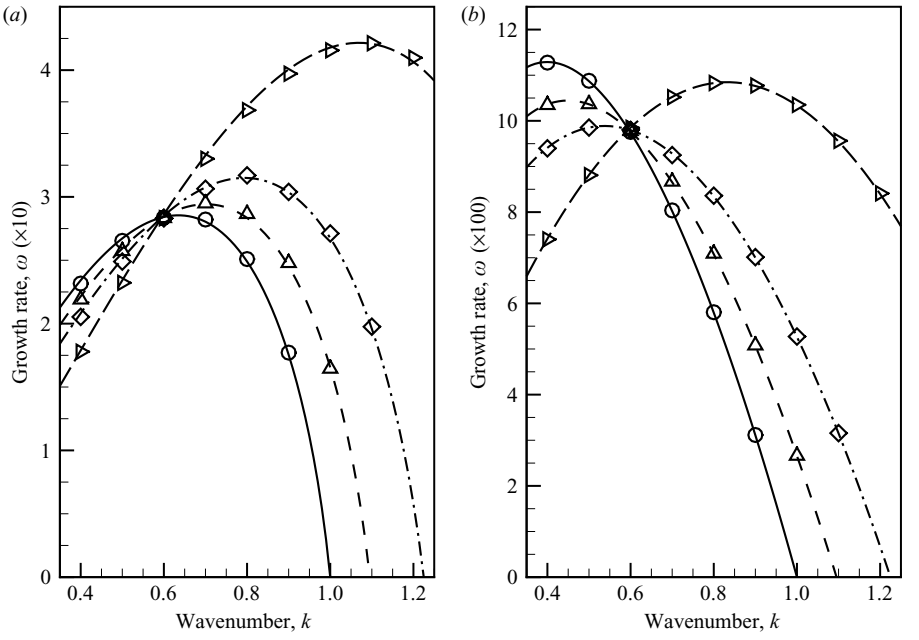

FIGURE 3. Wavenumber dependence of growth rates. Growth rates from linear theory (lines) are shown along with computed growth rates obtained from two-dimensional simulations (symbols) for (*a*) moderately viscous filaments of $N_{Oh} = 0.1$ and (*b*) viscous filaments of $N_{Oh} = 1.0$ when $R = 10$ and $\varepsilon = 0.01$. Results are shown for $N_E = 0$ (——, ○), $N_E = 1$ (- - -, △), $N_E = 2$ - · -, ◇) and $N_E = 4$ (– –, ▷).

the maximum growth rate for an uncharged filament increases with decreasing N_{Oh}, asymptotically approaching Rayleigh's (1879) result of $k_{max} \approx 0.697$ in the inviscid limit. The nature of electrostatic stresses as described above require for a given N_{Oh} that k_{max} increases with increasing N'_E.

To compare results from the one- and two-dimensional algorithms to the dispersion relation described by (3.1) and (3.3), the growth rate ω of the surface disturbance predicted by the simulations is determined as described in Appendix C. Figures 3 and 4 compare computed growth rates from two-dimensional simulations with those obtained from the dispersion relation described by (3.1) and (3.3). Excellent agreement between the two techniques is demonstrated over a wide range of the parameter space. The largest deviations ($\sim$1 %) between the simulations and linear theory occur in the lower limit of the range of Ohnesorge numbers examined ($N_{Oh} \sim 0.01$), and much better agreement (<0.1 %) is observed at higher N_{Oh}. A similar trend is reported by Ashgriz & Mashayek (1995) for uncharged jets. This level of agreement lends strong support to the accuracy of the two-dimensional algorithm. Figure 3 shows the variation of growth rates with wavenumber both for uncharged ($N_E = 0$) jets and charged jets of various N_E for moderately viscous jets of $N_{Oh} = 0.1$ and viscous jets of $N_{Oh} = 1.0$. A number of the features of the dispersion relation described above are apparent from figure 3, including the increase of k_{crit} and k_{max} with increasing N_E, the existence and location of k_E, and the stabilizing (destabilizing) influence of electrostatic stresses for $k < k_E$ ($k > k_E$) which becomes more pronounced with increasing N_E. Further, a comparison of figures 3(*a*) and 3(*b*) shows that, at each N_E, k_{max} is larger in the less viscous case. The influence of N_{Oh} on growth rates ω for

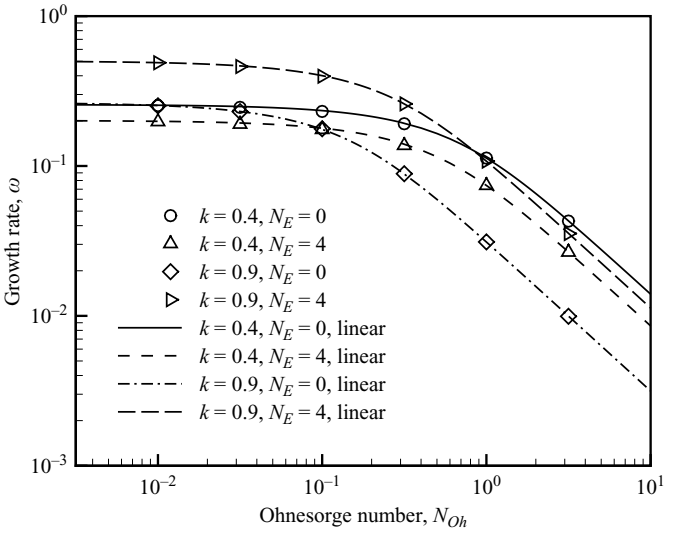

FIGURE 4. Ohnesorge number dependence of growth rates. Growth rates from linear theory (lines) are compared with results obtained from two-dimensional simulations (symbols) for a wide range of N_{Oh} when $R = 10$ and $\varepsilon = 0.01$ for both uncharged filaments ($N_E = 0$) and charged filaments with $N_E = 4$.

fixed k and R is shown in figure 4. Results are shown for both $k > k_E (k = 0.9)$ and $k < k_E (k = 0.4)$. Examination of the dispersion relation shows that ω is independent of N_{Oh} as the inviscid limit is approached and is inversely proportional to N_{Oh} in the Stokes flow limit. Both of these limiting behaviours and the transition region between them are apparent from figure 4. Figure 4 also shows that electrostatic stresses are stabilizing for $k < k_E$ and destabilizing for $k > k_E$ for all N_{Oh}.

Growth rates obtained from one-dimensional simulations differ only negligibly from those obtained from two-dimensional simulations and from linear theory for the entire range of the parameter space examined. In this regard, the one- and two-dimensional algorithms are indistinguishable.

3.2. *Electrostatic stresses and breakup times*

In this subsection, the time t_b required for an electrified jet to break after the imposition of a disturbance of wavenumber k and amplitude ε predicted by simulations is compared to that obtained from linear theory. Here, t_b is defined as the time required for the minimum radius to fall below $h_{min} = 2 \times 10^{-3}$. In this paper, the effects of k, N_{Oh} and N_E on t_b are examined while holding ε fixed at $\varepsilon = 10^{-2}$.

Figure 5 shows the variation of computed breakup times obtained from two-dimensional simulations with wavenumber for (*a*) moderately viscous jets of $N_{Oh} = 0.1$ and (*b*) viscous jets of $N_{Oh} = 1.0$. Results are shown both for uncharged jets ($N_E = 0$) and for charged jets of various N_E. Breakup times from linear theory, obtained from the dispersion relation defined in § 3.1, are included for comparison (i.e. $t_b = -\log(\varepsilon)/\omega$). Figure 5 shows that the computed breakup times from two-dimensional simulations exhibit the same qualitative trends expected from linear theory. In both the moderately viscous case and the viscous case, computed breakup times increase with N_E for longer waves and decrease for shorter waves, with the transition occurring in the vicinity of $k_E \approx 0.6$, though in the viscous case the transition occurs at a slightly larger wavenumber. Similar results are reported by López-Herrera *et al.* (2005). The

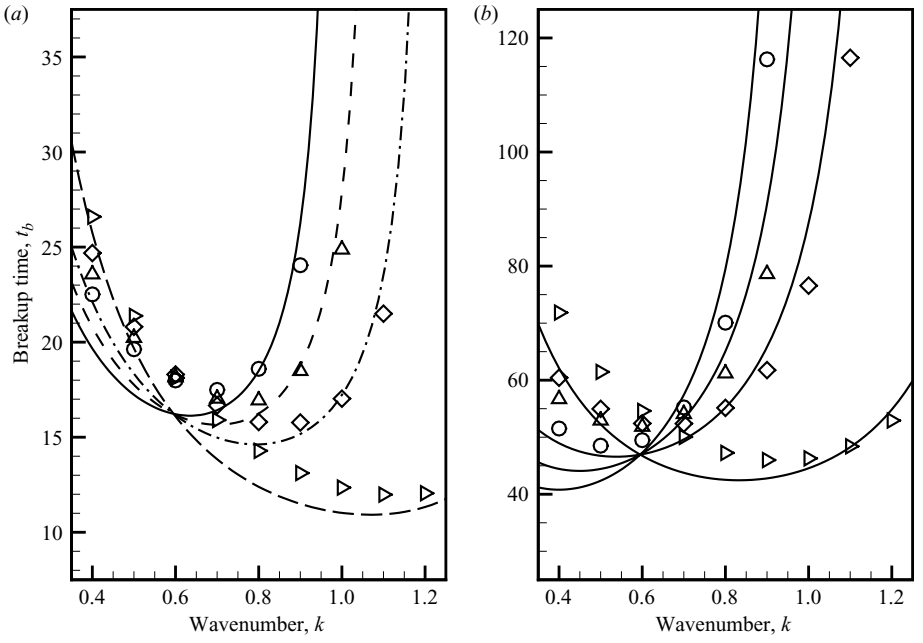

FIGURE 5. Influence of electrostatic stresses on jet breakup times t_b. The variation of breakup times with axial wavenumber k for (a) moderately viscous jets of $N_{Oh} = 0.1$ and (b) viscous jets of $N_{Oh} = 1.0$ is shown for uncharged ($N_E = 0$) jets and for charged jets of various N_E. Breakup times obtained from two-dimensional simulations (symbols) are shown along with results from linear theory (lines). Results are shown for $N_E = 0$ (——, ○), $N_E = 1$ (- - -, △), $N_E = 2$ (- · - , ◇) and $N_E = 4$ (– –, ▷).

wavenumber k_{max} associated with the fastest breakup time is larger in the moderately viscous case than in the viscous case for all N_E. Further, k_{max} increases monotonically with N_E in both cases, as does k_{crit}. A quantitative comparison of computed breakup times with linear theory shows that, for both viscous and slightly viscous jets, the computed breakup times from two-dimensional simulations are somewhat larger than the breakup times obtained from linear theory for long waves and are somewhat smaller than the breakup times obtained from linear theory for short waves. This trend is observed for all N_{Oh} and N_E examined. The best agreement is obtained for wavenumbers slightly larger than the k_{max} determined from linear theory for each N_{Oh} and N_E. The same phenomenon is reported by Ashgriz & Mashayek (1995) in their study of uncharged jets.

Figures 6 and 7 show the variation of computed breakup times obtained from two-dimensional simulations with N_E for moderately viscous filaments of $N_{Oh} = 0.1$ and viscous filaments of $N_{Oh} = 1.0$, respectively, for several wavenumbers. Breakup time predictions from linear theory are included for comparison. Recall that linear theory requires that there be no electrostatic influence on the dynamics of the filament, and hence on the breakup time, for $k_E \approx 0.6$, as may be seen in figures 6(c) and 7(c). Although linear theory tends somewhat to underestimate breakup times in this range of wavenumbers, for low to moderate values of N_E, breakup times obtained from two-dimensional simulations follow generally the trends expected from linear theory: computed breakup times increase monotonically with N_E for $k < k_E$, remain essentially unchanged with N_E for $k \approx k_E$, and decrease monotonically with N_E for $k > k_E$. At higher N_E, however, these trends begin to break down as nonlinear effects

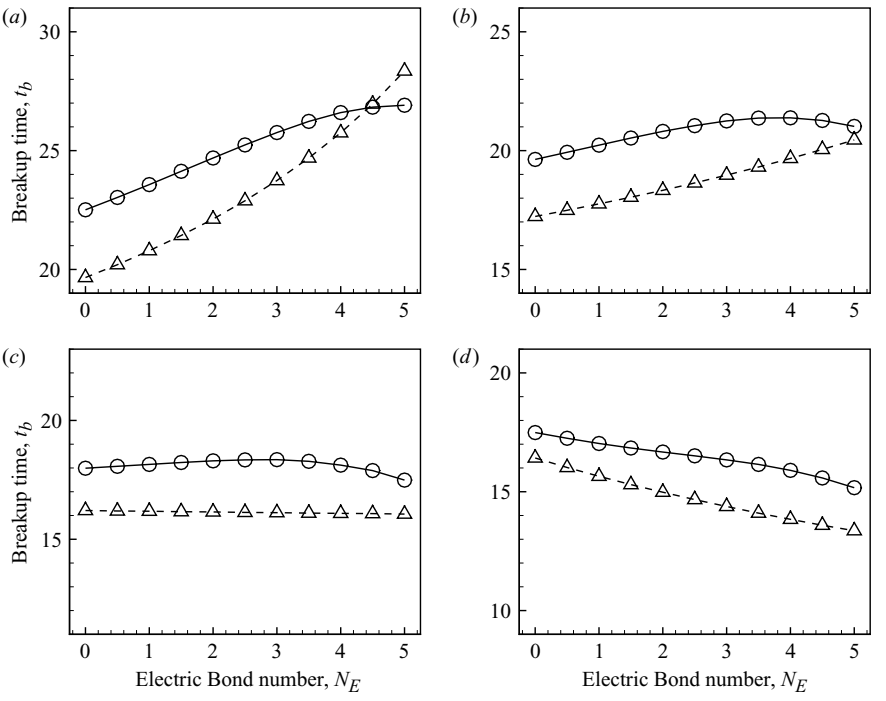

FIGURE 6. Influence of electrostatic stresses on jet breakup times t_b. Breakup times for moderately viscous jets of $N_{Oh} = 0.1$ from two-dimensional simulations are shown for wavenumbers in the vicinity of $k_E \approx 0.6$ at various N_E alongside t_b predicted from linear theory when $R = 10$. For low to moderate electric stresses, trends in t_b follow the expectations of linear theory, while in the limit of high N_E nonlinear effects become increasingly more important. (*a*) $k = 0.4$, (*b*) 0.5, (*c*) 0.6, (*d*) 0.7. ○, two-dimensional algorithm; △, linear theory.

become increasingly important. This is not too surprising, as satellite drops grow larger and begin to develop earlier for highly charged jets than for uncharged or moderately charged jets, while primary drops elongate radially more quickly and to a greater extent at higher N_E. Neither of these characteristics of highly charged jet breakup can be accounted for by linear theory.

A comparison of breakup times t_b obtained from two-dimensional and one-dimensional simulations indicates that the one-dimensional algorithm does reasonably well in predicting breakup times. Figure 8 shows how t_b obtained from two- and one-dimensional simulations varies with N_E for (*a*) moderately viscous jets of $N_{Oh} = 0.1$ and (*b*) viscous jets of $N_{Oh} = 1$. Breakup times from linear theory are included for comparison. While the one-dimensional algorithm tends to underestimate breakup times slightly in the moderately viscous case relative to the more accurate two-dimensional algorithm, the variation of computed breakup times with N_E is substantially similar for both algorithms. In the viscous case, the two algorithms agree strikingly well at lower Bond numbers ($N_E < 2$), although there are significant deviations at higher N_E.

3.3. *Influence of electrode radius*

Results from two-dimensional simulations indicate that $R = 10$ is sufficiently large that further increases in R do not significantly effect the dynamics of jet breakup for the ranges of k, N_E and N_{Oh} examined in this work ($k \geqslant 0.3$, $0 \leqslant N_E \leqslant 5$, $0.001 \leqslant N_{Oh} \leqslant 10$).

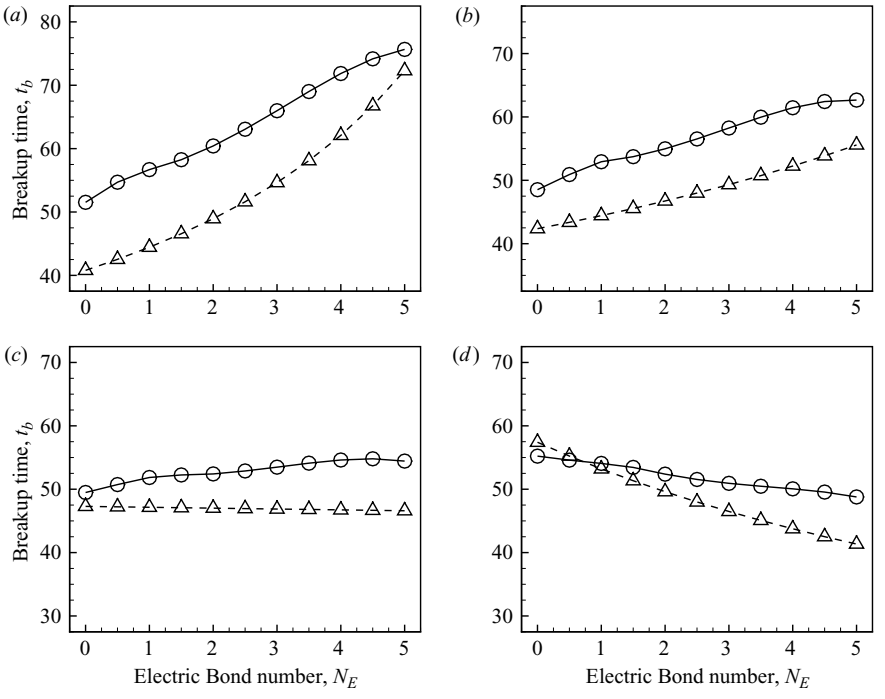

FIGURE 7. Same as figure 6 except for viscous jets of $N_{Oh} = 1.0$.

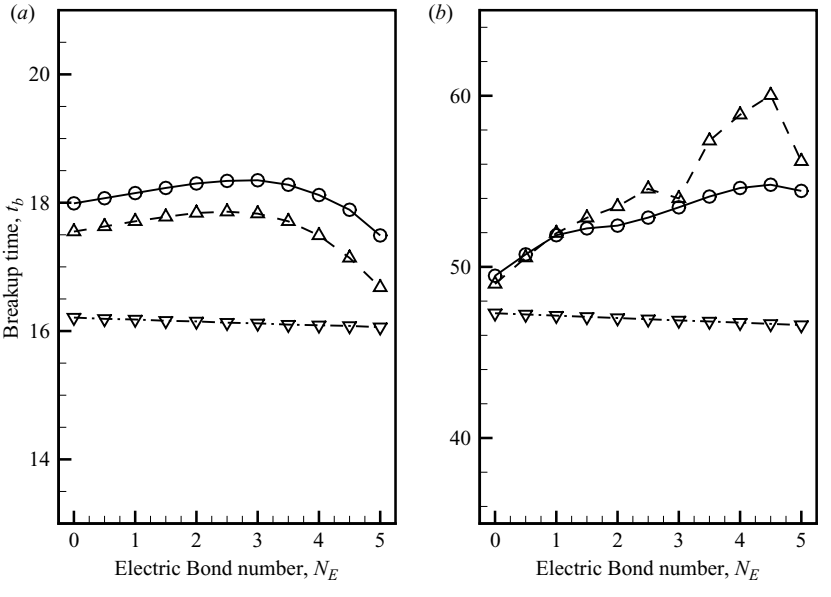

FIGURE 8. Comparison of breakup times predicted by the △, one- and ○, two-dimensional algorithms. Breakup times for (*a*) moderately viscous jets of $N_{Oh} = 0.1$ and (*b*) viscous jets of $N_{Oh} = 1.0$ from one- and two-dimensional simulations are shown for jets subjected to perturbations of wavenumber $k = 0.6$ for a range of electric Bond numbers when $R = 10$. Breakup times obtained from linear theory, ▽, are shown for comparison. Considerably better agreement between the two algorithms is observed for the moderately viscous case.

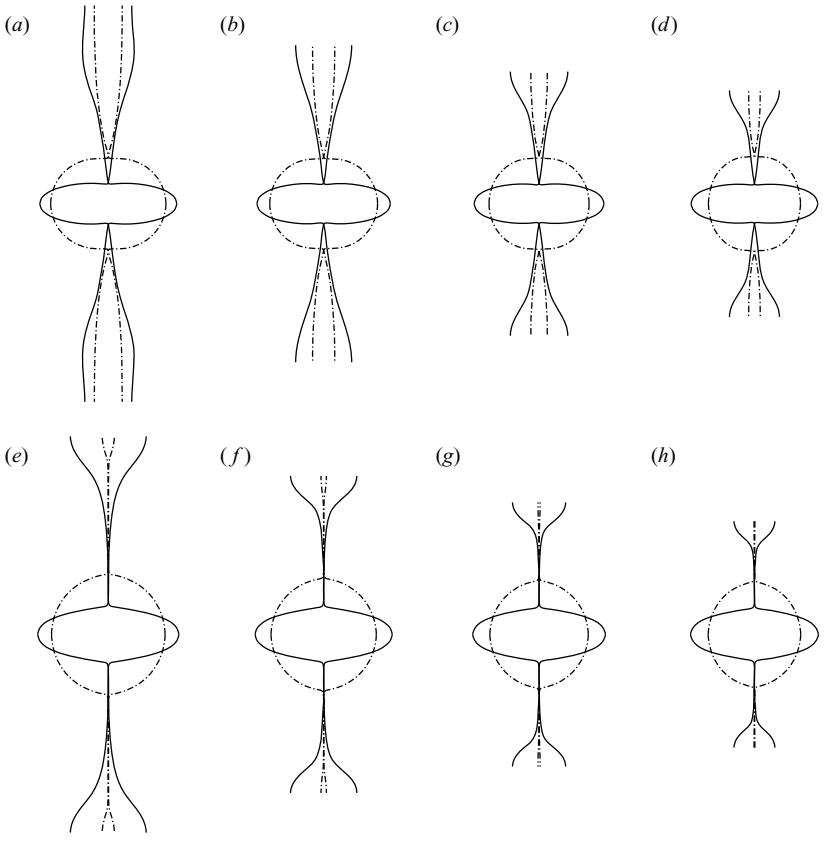

FIGURE 9. Influence of electrostatic stresses on jet profiles at the incipience of pinch-off for moderately viscous jets of $N_{Oh} = 0.1$ (*a–d*) and viscous jets of $N_{Oh} = 1$ (*e–h*). Computed jet profiles from two-dimensional simulations are shown for both uncharged (— · —) jets, $N_E = 0$, and charged (——) jets, $N_E = 5$, at $h_{min} = 0.002$ for (*a*, *e*) $k = 0.4$, (*b*, *f*) $k = 0.5$, (*c*, *g*) $k = 0.6$ and (*d*, *h*) $k = 0.7$.

Thus, for all subsequent results shown, the value of the electrode radius is fixed at $R = 10$.

3.4. *Electrostatic stresses and drop formation*

Figure 9 highlights a number of features of drop formation from breakup of electrified jets. In Figure 9(*a–d*), computed jet profiles at the incipience of pinch-off from two-dimensional simulations are shown for moderately viscous jets of $N_{Oh} = 0.1$ for a sequence of wavenumbers. Figure 9(*e–h*) shows jet profiles for the same sequence of wavenumbers but for viscous jets of $N_{Oh} = 1$. Profiles for uncharged jets, i.e. for $N_E = 0$, indicated by the dash-dot curves, are shown superimposed on profiles for charged jets ($N_E = 5$), indicated by the solid curves. The jet profiles are shown over an axial distance corresponding to a full wavelength, λ, centred about $z = 0$. Perhaps the most significant and obvious differences between the uncharged and charged jet profiles shown in these figures relate to the morphology of the drops formed at pinch-off. In this work, the ligaments which connect the large primary drops (centrally located in the profiles shown) at the incipience of pinch-off are referred to as satellite drops, following the convention of Ashgriz & Mashayek (1995), though it should be recognized that these ligaments can either recoil after the initial pinch-off to form a

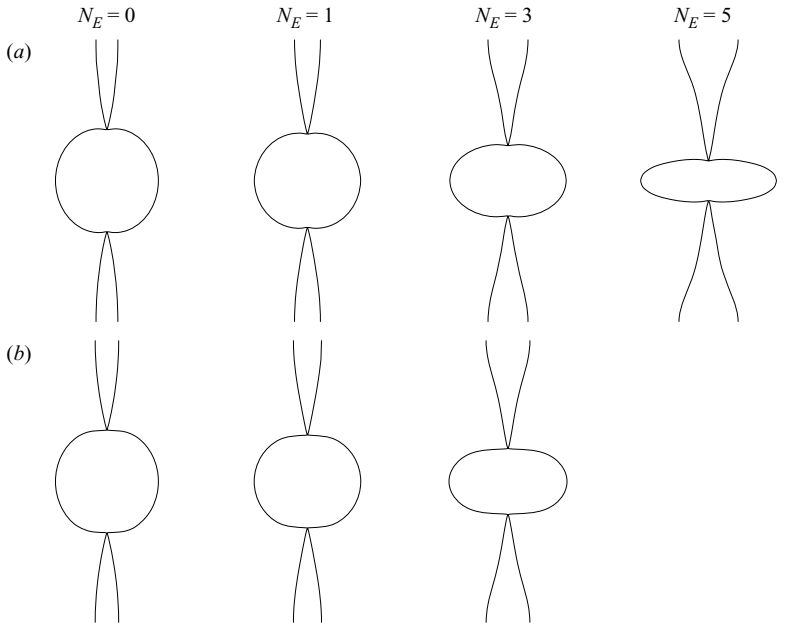

FIGURE 10. Comparison of computed jet profiles from one- and two-dimensional simulations at the incipience of pinch-off. Here, jet profiles obtained from (*a*) two-dimensional simulations and (*b*) one-dimensional simulations are shown for slightly viscous jets of $N_{Oh} = 0.01$ subjected to perturbations of wavenumber $k = 0.6$ at $h_{min} = 0.002$. Note that the one-dimensional algorithm fails prior to reaching $h_{min} = 0.002$ for $N_E = 5$.

single satellite drop or break up to form a series of smaller satellite drops. Figure 9 shows that the primary drops formed from charged jets are smaller and significantly more oblate or radially elongated than the primary drops formed from uncharged jets of the same N_{Oh} and k. Furthermore, the satellite drops formed from charged jets are significantly larger than the satellite drops formed from uncharged jets of the same N_{Oh} and k. These phenomena have been observed for all combinations of N_E, N_{Oh} and k examined in this work and appear to be universal features of electrified jet breakup. Furthermore, these phenomena become more pronounced as N_E is increased (see below). The satellite drops formed at pinch-off from uncharged, moderately viscous jets, which are relatively large, exhibit cone-like structures that taper smoothly toward the pinch-points and connect to the primary drops through very short, thin thread-like structures. The satellite drops formed from charged, moderately viscous jets, retain these structures, but also feature large, bulbous central regions which constitute most of the volume of these satellites. The primary drops formed at pinch-off from uncharged viscous jets are connected by thin thread-like satellites which exhibit small bulbous cores at larger wavelengths, though these structures are absent at shorter wavelengths. With charged viscous jets, however, the satellite drops formed at pinch-off exhibit large bulbous central regions at all wavelengths (similar to those observed with charged, moderately viscous jets) which are connected to the primary drops by long thread-like structures that are very similar to those observed in the uncharged case.

To assess the accuracy of the one-dimensional algorithm, it is instructive at this point to compare the shapes of the drops formed at pinch-off computed from one-dimensional simulations with results from two-dimensional simulations. Figures 10 to 12 compare computed profiles of uncharged and charged jets at the incipience of

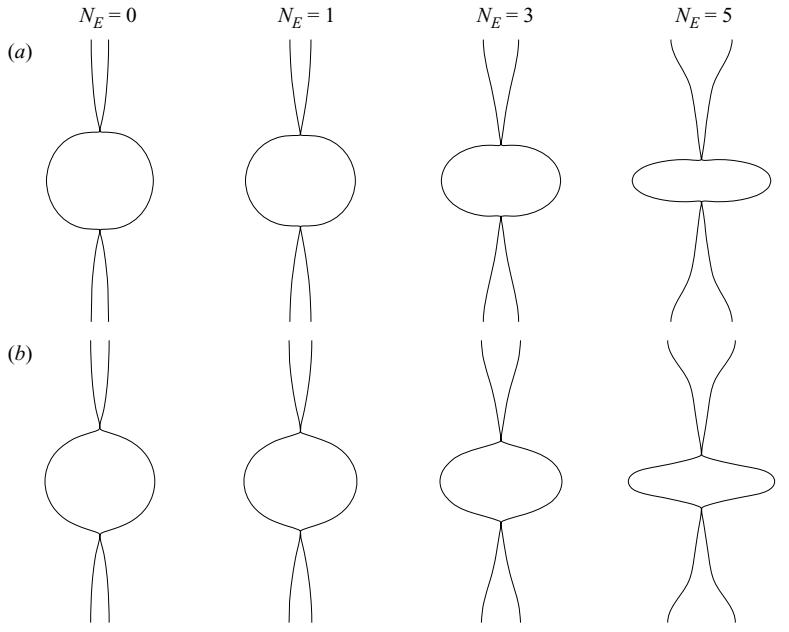

FIGURE 11. Same as figure 10 except for moderately viscous jets of $N_{Oh} = 0.1$.

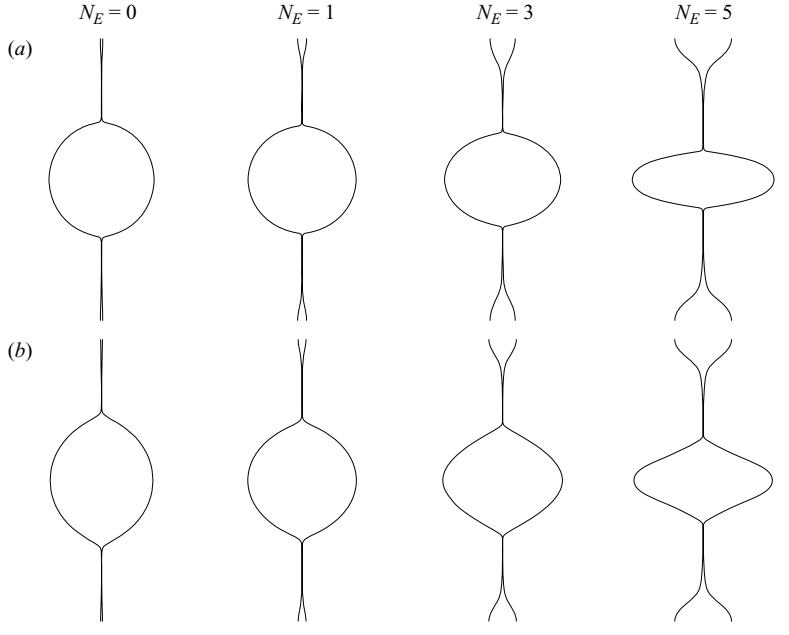

FIGURE 12. Same as figure 10 except for viscous jets of $N_{Oh} = 1.0$.

pinch-off obtained from two-dimensional simulations with computed jet profiles from one-dimensional simulations for slightly viscous jets of $N_{Oh} = 0.01$, moderately viscous jets of $N_{Oh} = 0.1$, and viscous jets of $N_{Oh} = 1.0$, respectively. These figures demonstrate that the one-dimensional algorithm reproduces reasonably well the qualitative and gross features of jet profiles obtained from the two-dimensional algorithm. The

agreement between the two algorithms is generally better for uncharged jets and charged jets at low N_E than for charged jets at higher N_E. The largest deviations occur in the vicinity of the pinch point. In the slightly viscous case, for example, overturning of the interface of the primary drop near the pinch point, a phenomenon which has been reported by others examining pinch-off singularities both in the inviscid limit (Chen & Steen 1997; Day, Hinch & Lister 1998) and with Newtonian fluids at low N_{Oh} (Wilkes *et al.* 1999; Chen *et al.* 2002), is observed with profiles from two-dimensional simulations, but not with profiles from one-dimensional simulations. This deviation is to be expected, as the one-dimensional algorithm requires that the free surface be described as a single-valued function of the axial coordinate (see § 2.2) and hence artificially precludes interface overturning. The influence of electrostatic stresses on interface overturning is discussed at length in § 3.5. In the viscous case, and to a lesser extent in the moderately viscous case, the computed jet profiles from one-dimensional simulations exhibit an anomalous tapering of the primary drop toward the pinch point which is not observed in computed jet profiles from two-dimensional simulations and which is more pronounced at higher electric Bond numbers. While the primary drop profiles predicted by the one-dimensional algorithm show an increased radial elongation with increasing N_E in the viscous case, as do their counterparts predicted by the two-dimensional algorithm, the shapes of the primary drops predicted by the one-dimensional algorithm at high N_E are visibly more bulb-like than those predicted by the two-dimensional algorithm, which are shaped roughly like oblate spheroids. A comparison of the sizes and shapes of the satellite drops predicted by the two algorithms yields far better agreement.

3.4.1. *Electrostatic stresses and primary/satellite drop sizes*

In the absence of electrostatic stresses, Ashgriz & Mashayek (1995) have shown that the sizes of the primary and satellite drops formed at pinch-off decrease with increasing wavenumber and that the satellite drop size is smaller for a more viscous jet than for a less viscous jet subjected to a perturbation of the same wavenumber. The influence of electrostatic stresses on computed primary and satellite drop sizes is highlighted in figures 13 to 15. The results shown in these figures are from two-dimensional simulations and report drop sizes in terms of radii of spheres having the same volumes as the drops. Figure 13 shows how the computed sizes of the primary drops and satellite drops formed at pinch-off vary with k at various N_E for moderately viscous jets of $N_{Oh} = 0.1$ and viscous jets of $N_{Oh} = 1$. For both moderately viscous and viscous jets, computed primary and satellite drop sizes decrease monotonically with increasing k at all N_E. Further, primary (satellite) drop sizes decrease (increase) with increasing N_E at fixed k and N_{Oh}. For satellite drops, this trend is more pronounced for viscous jets than for moderately viscous jets. For primary drops, however, the opposite is true, as satellite drops are uniformly larger at fixed N_E and k for moderately viscous jets than for viscous jets. Similar trends are reported by López-Herrera *et al.* (1999) and López-Herrera & Gañan-Cálvo (2004). Figure 14 shows how the computed sizes of the primary and satellite drops formed at pinch-off vary with N_E for various wavenumbers, with results reported for both moderately viscous and viscous jets. In both cases, the computed size of satellite drops increases nearly linearly with N_E for fixed k and N_{Oh} in the range of N_E examined, while the computed primary drop size decreases monotonically with N_E. Further, primary drop size dependence on k diminishes with increasing N_E. Figure 15 shows the electric Bond number dependence of computed primary and satellite drop sizes for jets of various N_{Oh} at fixed wavenumber ($k = 0.6$). Computed primary (satellite) drop sizes

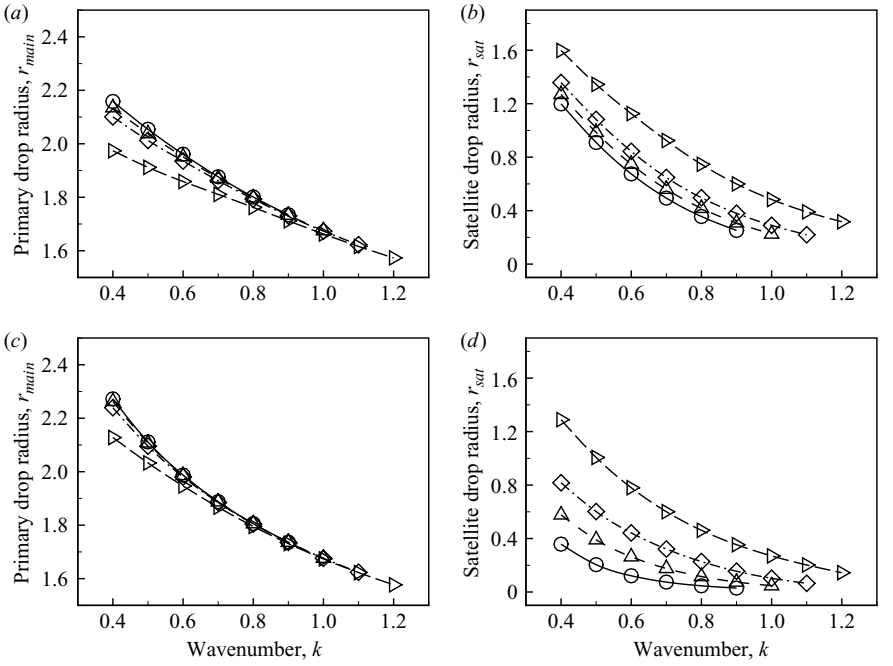

FIGURE 13. Influence of electrostatic stresses on primary and satellite drop size. The variation of the sizes of the primary and satellite drops formed at pinch-off with wavenumber are shown for ○, uncharged ($N_E = 0$) jets and for charged jets with △, $N_E = 1$; ◇, $N_E = 2$; and ▷, $N_E = 4$. Results are shown for both moderately viscous jets of $N_{Oh} = 0.1$, (a, b), and viscous jets of $N_{Oh} = 1$, (c, d).

are larger (smaller) for more viscous jets than for less viscous ones for uncharged jets ($N_E = 0$) and for charged jets at all N_E.

Drop volumes computed using the one-dimensional algorithm agree reasonably well with their counterparts computed using the two-dimensional algorithm. Figure 16 compares computed primary (a) and satellite (b) drop sizes, reported as radii of equivalent spheres, obtained from two- and one-dimensional simulations for moderately viscous jets of $N_{Oh} = 0.1$ and viscous jets of $N_{Oh} = 1.0$ over a range of N_E at fixed wavenumber. While the one-dimensional algorithm tends to underestimate slightly the primary drop volumes and to overestimate slightly the satellite drop volumes relative to the two-dimensional algorithm for the moderately viscous jets, the same qualitative behaviour, i.e. a monotonic decrease (increase) in primary (satellite) drop volumes with increasing N_E, is observed with both algorithms. Better agreement between the two algorithms is observed in the viscous case, particularly at low N_E.

López-Herrera *et al.* (1999) report that satellite sizes increase with N_E for the region of the parameter space that they examined with their slender-jet algorithm. For the range of wavenumbers examined in that work ($k > 0.57$), these authors report good agreement with the inviscid analysis of Setiawan & Heister (1997) for $N_E = 2.5$ and $R = 10$. Setiawan & Heister report that satellite volumes increase with N_E for short waves in the inviscid case, but actually decrease with N_E for long waves, with the transition wavenumber demarcating the two regimes increasing with N_E. A jet profile near pinch-off is shown in that work for a highly charged ($N_E = 5$) jet subjected to a perturbation of large wavelength, $k = 0.4$, when $R = 10$. The profile shows a very small satellite drop and a primary drop that features a large central

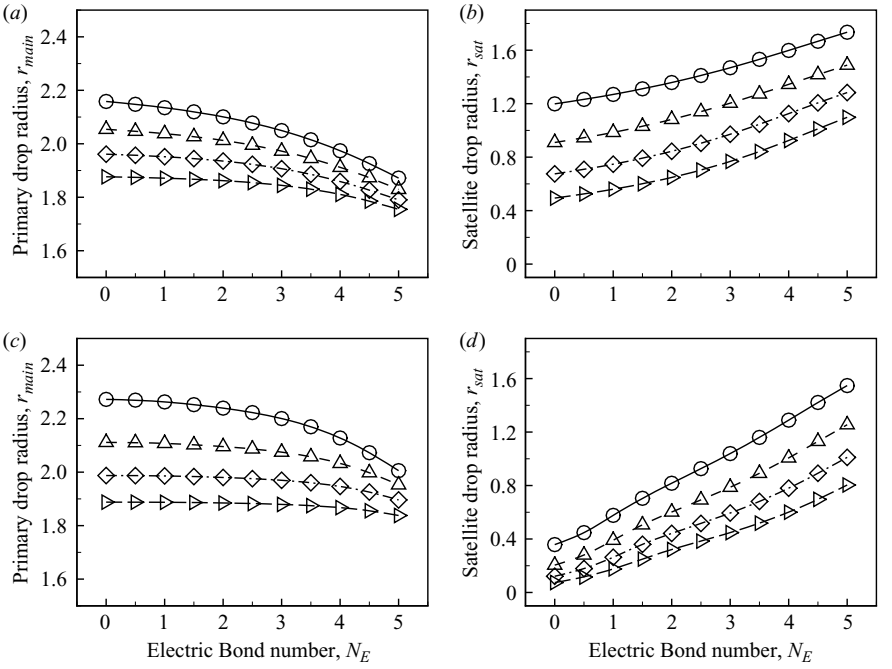

FIGURE 14. Influence of electrostatic stresses on primary and satellite drop size. The variation of the sizes of the primary and satellite drops formed at pinch-off with electric Bond number are shown for jets subjected to perturbations of various wavenumbers. Results are shown for both moderately viscous jets of $N_{Oh} = 0.1$, (a, b), and viscous jets of $N_{Oh} = 1$, (c, d). ○, $k = 0.4$; △, 0.5; ◇, 0.6; ▷, 0.7.

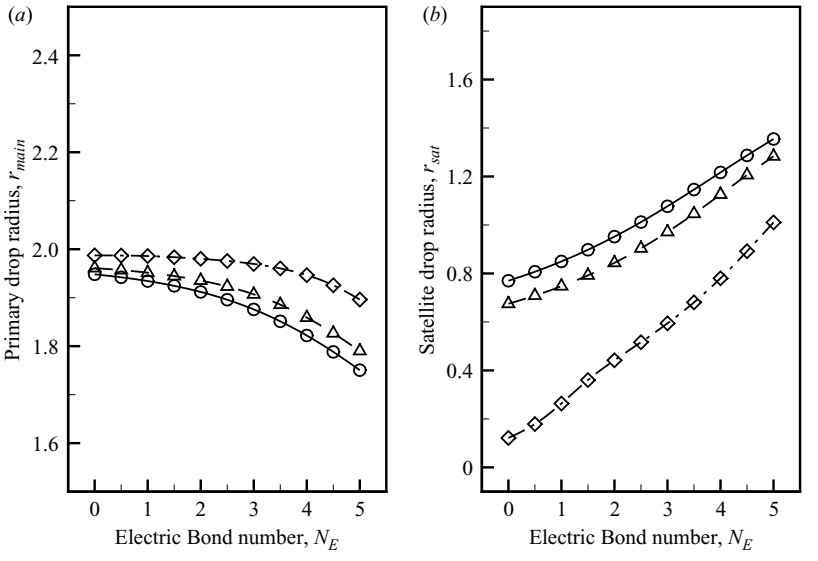

FIGURE 15. Influence of electrostatic stresses on primary and satellite drop size. The variation of the sizes of the (a) primary and (b) satellite drops formed at pinch-off with electric Bond number are shown for jets subjected to perturbations of wavenumber $k = 0.6$. Results are shown for ○, slightly viscous jets of $N_{Oh} = 0.01$; △, moderately viscous jets of $N_{Oh} = 0.1$; and ◇, viscous jets of $N_{Oh} = 1.0$.

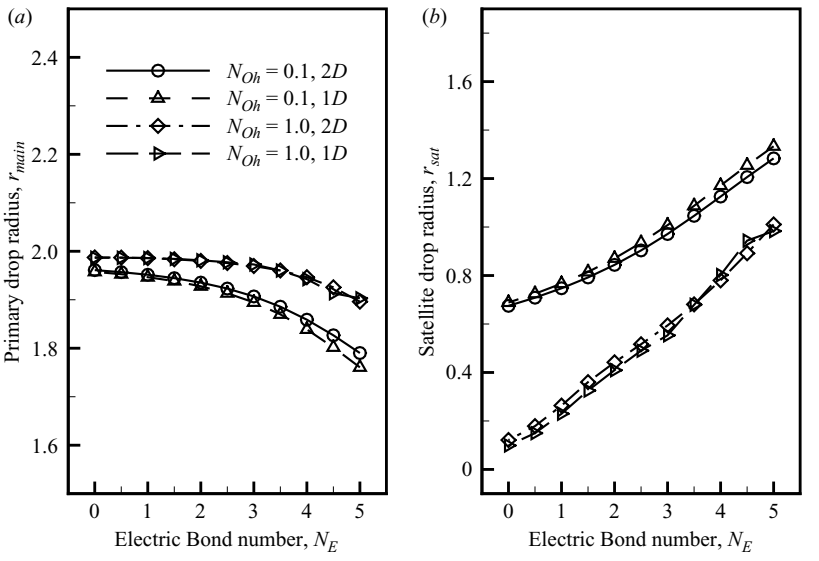

FIGURE 16. Comparison of primary and satellite drop sizes predicted from one- and two-dimensional ($1D$ and $2D$) simulations. The variation of the sizes of (a) primary and (b) satellite drops formed at pinch-off predicted from one- and two-dimensional simulations with electric Bond number are shown for jets subjected to perturbations of wavenumber $k = 0.6$. Results are shown for both moderately viscous jets of $N_{Oh} = 0.1$ and viscous jets of $N_{Oh} = 1.0$.

peak separated by troughs from two additional large peaks located symmetrically about $z = 0$. Simulations of highly charged jets subjected to perturbations of large wavelengths using the two-dimensional algorithm developed in this work do not support these observations. Figure 17 shows jet profiles near pinch-off for uncharged ($N_E = 0$) and highly charged ($N_E = 5$) jets subjected to long-wave perturbations with $k = 0.4$ spanning a large range of N_{Oh}. For each N_{Oh}, the satellite drop is significantly larger in the highly charged case than in the uncharged case. Note that for the highly charged jets, the primary drops do not exhibit multiple peaks but have the same oblate shape as is observed for highly charged shorter wave jets (see, for example, figure 9). While undulations on the surface of the satellite drops are visible for the slightly viscous ($N_{Oh} = 0.01$) and very slightly viscous ($N_{Oh} = 0.001$) jet profiles for $N_E = 5$, these undulations do not grow at a rate sufficient to produce the sorts of jet profiles reported by Setiawan & Heister even in the very slightly viscous case.

3.4.2. *Electrostatic stresses and drop charge at pinch-off*

The stabilities of the primary and satellite drops formed at pinch-off from the breakup of an electrified jet depend both on their sizes and shapes and on the charges that they carry. To assess the stability of these drops, following López-Herrera *et al.* (1999) and López-Herrera & Gañan-Cálvo (2004), we report here the ratio of the charge Q borne by the primary or satellite drop at pinch-off to the value of the charge that is borne by a spherical drop at the Rayleigh (1882) limit of stability, which is hereinafter referred to as the Rayleigh charge limit, Q_R, in lieu of the charges on the drops themselves. In terms of the dimensionless groups used in this work, $Q_R = \sqrt{96\pi N_E V}$, where V represents the dimensionless drop volume. A spherical drop, bearing charge in excess of Q_R, is unstable because the destabilizing

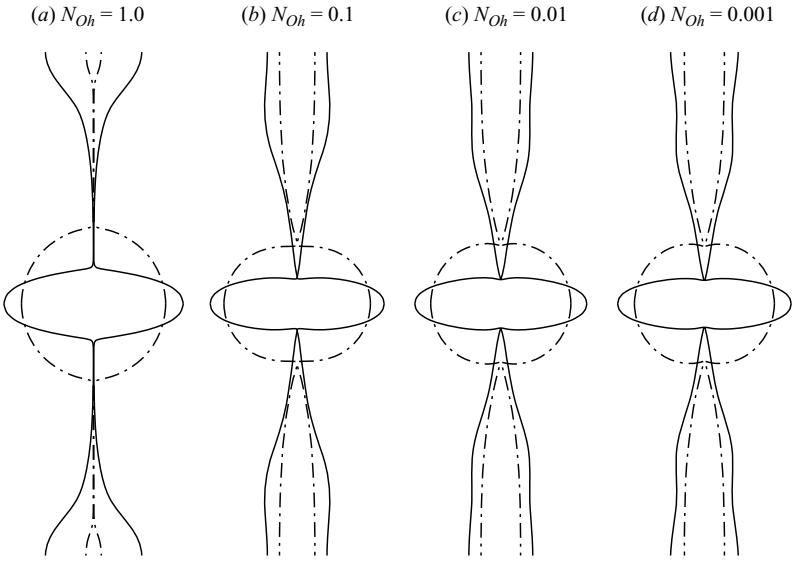

FIGURE 17. Influence of Ohnesorge number on profiles at pinch-off of jets that are subjected to long-wave perturbations, $k = 0.4$. Jet profiles are shown for uncharged jets ($- \cdot -$) and highly charged jets (——) when $N_E = 5$ for (*a*) $N_{Oh} = 1.0$, (*b*) $N_{Oh} = 0.1$, (*c*) $N_{Oh} = 0.01$ and (*d*) $N_{Oh} = 0.001$. The satellite drop is significantly larger for the charged jet than for the uncharged jet for all N_{Oh}.

effect of Coulombic charge repulsion is stronger than the stabilizing effect of surface tension. As the drops formed at pinch-off are highly deformed (particularly so for the satellite drops), a charge ratio of $Q/Q_R < 1$ does not guarantee the stability of the drops after pinch-off (Adornato & Brown 1983; Basaran & Scriven 1989). Rather, $Q/Q_R = 1$ represents an upper limit for Coulombic stability of the drops formed at pinch-off, and, for cases where $Q/Q_R > 1$, it is certain that the drops will eventually break up into two or more smaller drops.

Figure 18 shows the variation of computed charge ratios from two-dimensional simulations with wavenumber for the primary and satellite drops formed at pinch-off from both moderately viscous jets of $N_{Oh} = 0.1$ and viscous jets of $N_{Oh} = 1.0$ at various electric Bond numbers. The charge ratio for the primary drops, $(Q/Q_R)_{main}$, is relatively insensitive to k and N_{Oh}, but increases substantially as N_E is increased at fixed k. For the range of low to moderately high electric Bond numbers shown, however, the primary drops are Coulombically stable in both the moderately viscous case and the viscous case at all k. For moderately viscous jets, the charge ratio for satellite drops $(Q/Q_R)_{sat}$ increases with N_E at fixed k and decreases monotonically with increasing k at fixed N_E. This is due in part to a partial shielding of the satellite drops from the electric field caused by the proximity of the large primary drops. This shielding is more effective at larger wavenumbers simply because the satellite drops are shorter than those formed at smaller wavenumbers. These results are consistent with results reported by López-Herrera & Gañan-Cálvo (2004) for moderately viscous jets. With regard to viscous jets, the wavenumber dependence of $(Q/Q_R)_{sat}$ is somewhat more complex. Here, at low electric Bond numbers, $(Q/Q_R)_{sat}$ increases monotonically with k, whereas at higher electric Bond numbers, $(Q/Q_R)_{sat}$ exhibits a minimum; further, $(Q/Q_R)_{sat}$ typically decreases with N_E at fixed k in the viscous case. At low N_E, the satellite drops formed at pinch-off are similar in shape to

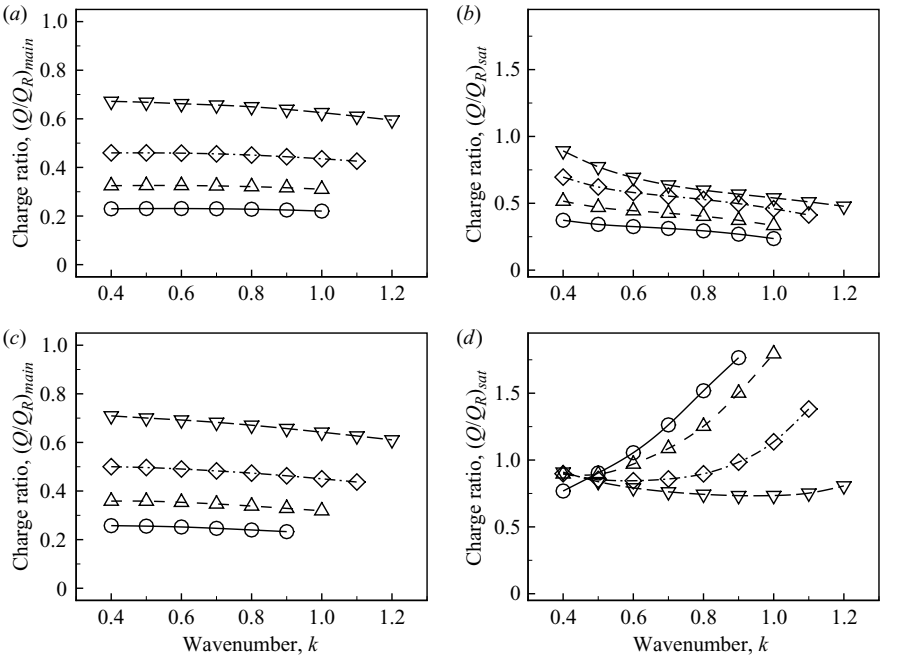

FIGURE 18. Influence of N_E on drop charge. ○, $N_E = 0.5$; △, 1.0; ◇, 2.0; ▽, 4.0. Here, the ratios of the charge on the primary drop and the satellite drop to the Rayleigh charge limit ($Q_R = \sqrt{96\pi N_E V}$) obtained from two-dimensional simulations are shown for moderately viscous jets of $N_{Oh} = 0.1$, (a, b), and viscous jets of $N_{Oh} = 1.0$, (c, d), for various N_E over a range of wavenumbers k.

satellite drops formed from uncharged jets (see, for example, figure 9). The satellites formed from jets at smaller wavenumbers have central bulbous cores which contain most of their volume. These structures are absent in satellite drops formed from jets with larger wavenumbers, which are are essentially long thread-like filaments. Because they lack central cores, these satellites have much larger surface to volume ratios than their counterparts formed from jets at larger wavenumbers. The combination of high surface charge density (a consequence of the slenderness of the thread-like satellites) and very high surface to volume ratio is extremely unstable, so that even with shielding provided by the proximity of the primary drops, $(Q/Q_R)_{sat}$ increases with k for viscous jets at low N_E. At higher N_E, the satellites formed at pinch-off from viscous jets have more substantial bulbous core structures at smaller wavenumbers, and small bulbous core structures are observed at larger wavenumbers; only at wavenumbers approaching k_{crit} do the satellite drops formed at pinch-off resemble long thread-like filaments. Thus, at higher N_E, $(Q/Q_R)_{sat}$ decreases with k at lower wavenumbers, as a consequence of the increased effectiveness of the shielding provided by the proximity of the primary drops, and increases with k at higher wavenumbers as a consequence of the thread-like structure of the satellites.

Figure 19 shows the variation of computed $(Q/Q_R)_{main}$ and $(Q/Q_R)_{sat}$ from two-dimensional simulations with electric Bond number at various wavenumbers for both moderately viscous jets of $N_{Oh} = 0.1$ and viscous jets of $N_{Oh} = 1$. In both cases, $(Q/Q_R)_{main}$ increases monotonically with N_E at all wavenumbers, and only a slight dependence on k is observed at fixed N_E. In the moderately viscous case, $(Q/Q_R)_{sat}$ increases monotonically with N_E for all wavenumbers and decreases with increasing

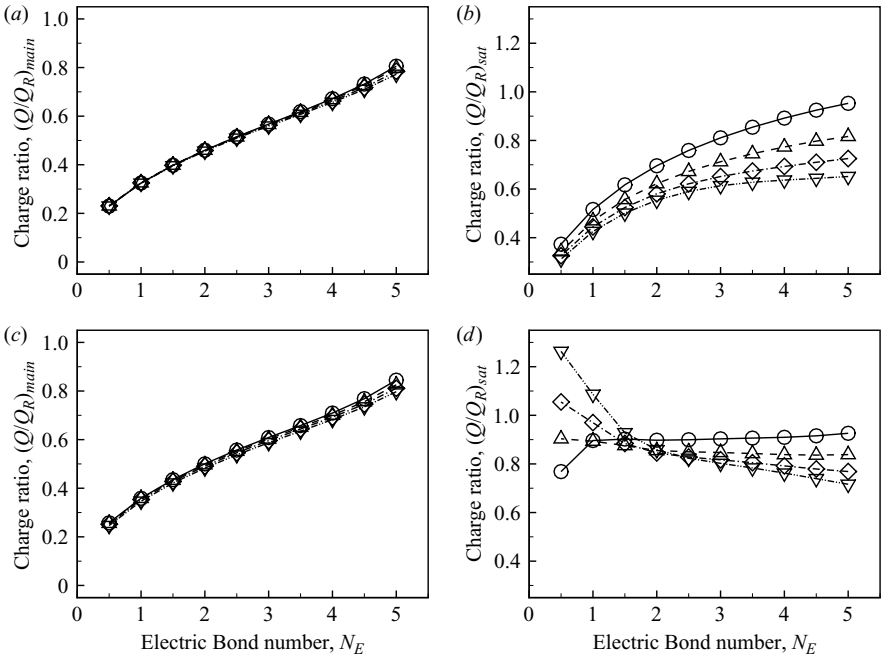

FIGURE 19. Influence of N_E on drop charge. ○, $k = 0.4$; △, 0.5; ◇, 0.6; ▽, 0.7. Here, the ratios of the charge on the primary drop and the satellite drop to the Rayleigh charge limit ($Q_R = \sqrt{96\pi N_E V}$) obtained from two-dimensional simulations are shown for moderately viscous jets of $N_{Oh} = 0.1$, (a, b), and viscous jets of $N_{Oh} = 1.0$, (c, d), for various wavenumbers over a range of electric Bond numbers.

k at fixed N_E. The variation of $(Q/Q_R)_{sat}$ with N_E is somewhat more complex in the viscous case, for reasons described above. For longer waves (e.g. $k = 0.4$), $(Q/Q_R)_{sat}$ increases dramatically at low N_E and levels off at higher N_E. For shorter waves (e.g. $k = 0.7$), $(Q/Q_R)_{sat}$ drops off rapidly with increasing N_E at lower electric Bond numbers and decreases more slowly at higher N_E. Figure 20 shows the variation of computed $(Q/Q_R)_{main}$ and $(Q/Q_R)_{sat}$ from two-dimensional simulations with N_E for slightly viscous jets of $N_{Oh} = 0.01$, moderately viscous jets of $N_{Oh} = 0.1$, and viscous jets of $N_{Oh} = 1$ when $k = 0.6$. The charge ratio for primary drops exhibits a moderate dependence on N_{Oh}; $(Q/Q_R)_{main}$ increases with N_{Oh} at fixed N_E for the range of N_E examined. The charge ratio for satellite drops increases monotonically with N_E for both slightly viscous jets and moderately viscous jets. This trend is reversed in the viscous case, as described above.

Charge ratios computed using the one-dimensional algorithm agree reasonably well with their counterparts from two-dimensional simulations. Figure 21 compares the electric Bond number dependence of the computed charge ratios for primary drops and satellite drops obtained from one- and two-dimensional simulations for both moderately viscous jets of $N_{Oh} = 0.1$ and viscous jets of $N_{Oh} = 1$ for perturbations of wavenumber $k = 0.6$. For moderately viscous jets, the one-dimensional algorithm tends to overestimate slightly $(Q/Q_R)_{main}$ and underestimate slightly $(Q/Q_R)_{sat}$, with better agreement between the two algorithms observed at lower N_E and larger deviations observed at higher N_E. For viscous jets, while there is little discernible difference between the two algorithms with respect to $(Q/Q_R)_{main}$, the one-dimensional algorithm tends to overestimate somewhat the charge ratio for satellite drops at low N_E.

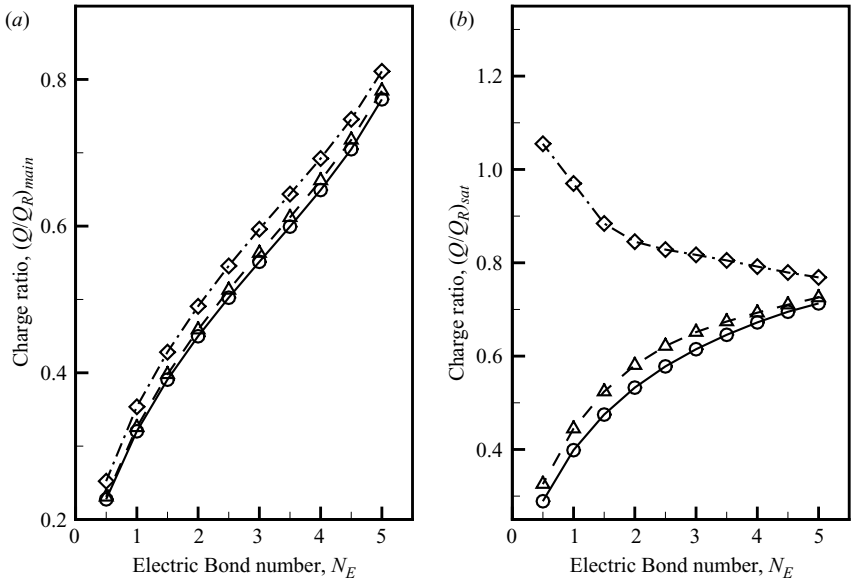

FIGURE 20. Influence of N_E on drop charge. Here, the ratios of the charge on (*a*) the primary drop and (*b*) the satellite drop to the Rayleigh charge limit ($Q_R = \sqrt{96\pi N_E V}$) obtained from two-dimensional simulations are shown for ○, slightly viscous jets of $N_{Oh} = 0.01$; △, moderately viscous jets of $N_{Oh} = 0.1$; and ◇, viscous jets of $N_{Oh} = 1.0$ subjected to perturbations of wavenumber $k = 0.6$ for a range of electric Bond numbers.

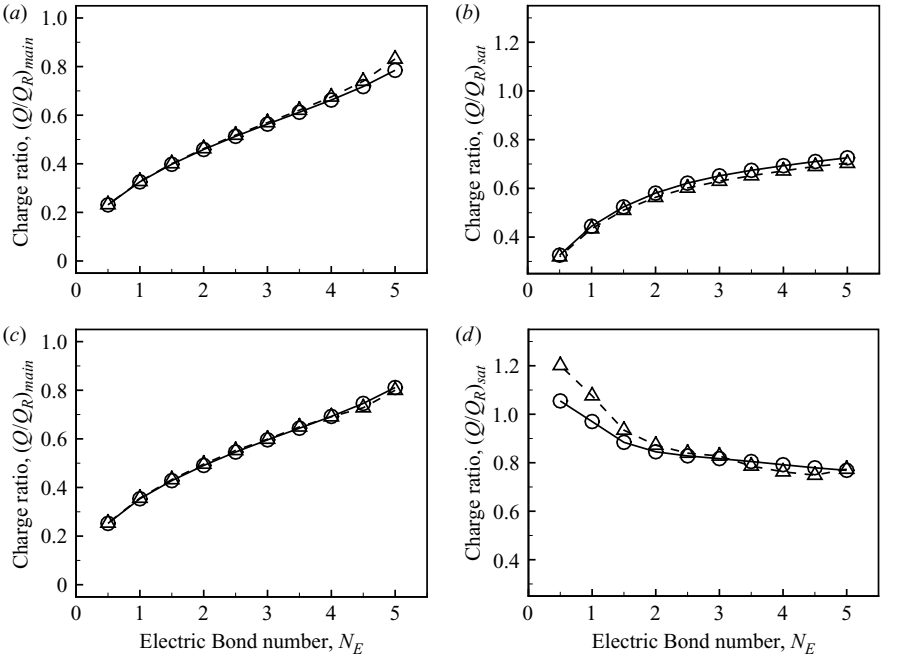

FIGURE 21. Comparison of drop charge from △, one- and ○, two-dimensional simulations. Here, the ratios of the charge on the primary drop and the satellite drop to the Rayleigh charge limit ($Q_R = \sqrt{96\pi N_E V}$) obtained from one- and two-dimensional simulations are shown for both moderately viscous jets of $N_{Oh} = 0.1$, (*a*, *b*), and and viscous jets of $N_{Oh} = 1$, (*c*, *d*), subjected to perturbations of wavenumber $k = 0.6$.

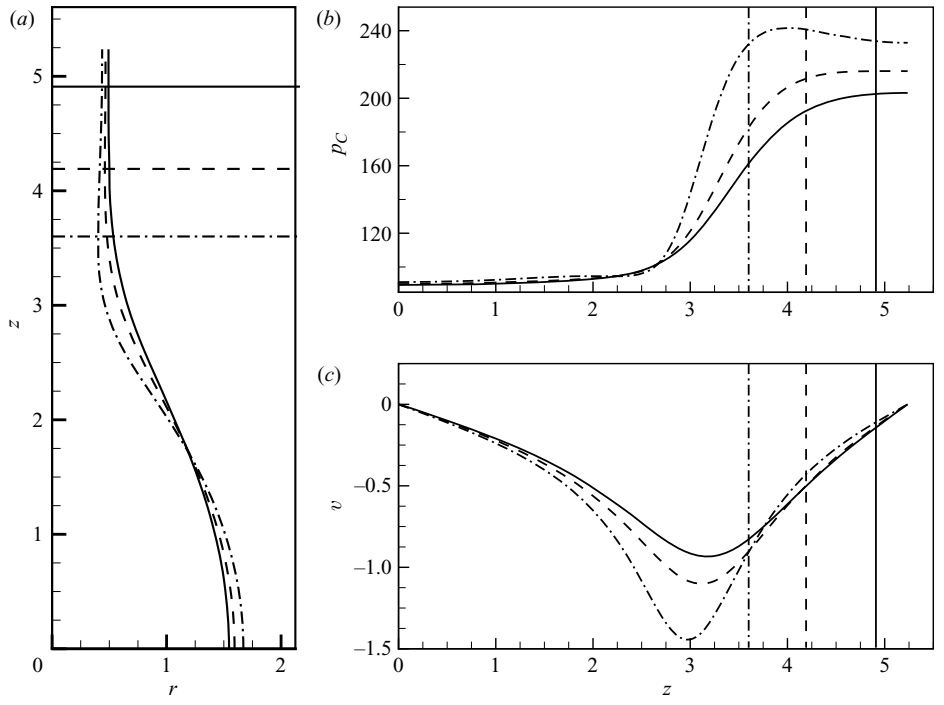

FIGURE 22. Influence of electrostatic stresses on satellite formation. Here, jet profiles, (*a*), are shown along with the axial variation of the capillary pressure, (*b*), and axial velocity evaluated along S_f, (*c*), for a sequence of instants during the evolution in time of an uncharged ($N_E = 0$) slightly viscous jet of $N_{Oh} = 0.01$ subjected to a perturbation of wavenumber $k = 0.6$. The axial location of h_{min} at each instant is indicated by the horizontal lines in (*a*) and by the vertical lines in (*b*) and (*c*). Profiles are shown at instants corresponding to $h_{min} = 0.493$ (——), $h_{min} = 0.461$ (- - -) and $h_{min} = 0.401$ (— · —).

3.4.3. *Electrostatic stresses and satellite drop formation*

To understand why the application of electrostatic stresses results in the formation of larger satellite drops, it is instructive first to consider the mechanism of satellite drop formation in uncharged jets. In the absence of electrostatic stresses ($N_E = 0$), the formation of satellite drops is driven by inertia (Eggers 1993; McGough & Basaran 2006). Initially, for small ε and $k < 1$, both the minimum radius h_{min} and the maximum capillary pressure are located at $z = \pi/k$. The capillary pressure gradient along the jet drives a flow of fluid from the neck, $z = \pi/k$, toward the swell, $z = 0$, depleting fluid from the neck. As the neck thins, the capillary pressure gradient increases, and the flow is accelerated. Because of symmetry, the axial velocity at $z = \pi/k$ is zero, and consequently the magnitude of the radially averaged axial velocity is a maximum at some axial location $z < \pi/k$. When inertia is significant, fluid is depleted faster in the vicinity of this point than in the vicinity of $z = \pi/k$. Eventually, this results in a transition from h_{min} being located at $z = \pi/k$ to h_{min} being located at an axial location $z = z_{min} < \pi/k$. The point at which this transition occurs signals the inception of the proto-satellite drop.

Figure 22 shows at several instants in the temporal evolution of an uncharged, slightly viscous jet of $N_{Oh} = 0.01$, highlighting the early stages of satellite drop development in a case for which a large satellite is observed to form at pinch-off (see figure 10). Jet profiles for half a wavelength (figure 22*a*) are shown at each instant

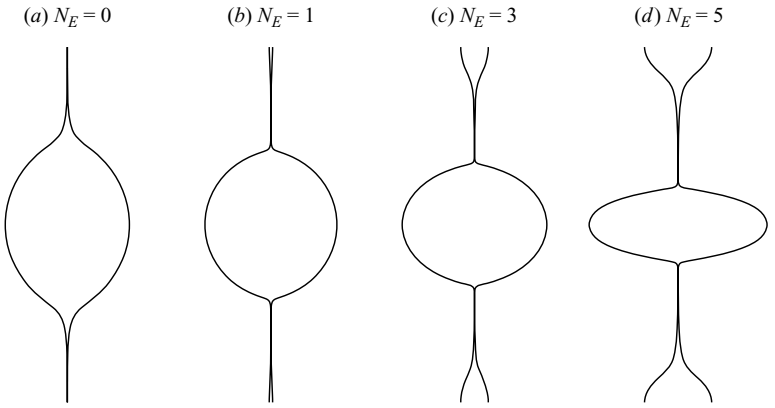

FIGURE 23. Influence of electrostatic stresses on jet profiles at the incipience of pinch-off for jets in the Stokes flow limit. Here, $k = 0.6$. For the uncharged jet, (*a*), the primary drop is prolate and the pinch-off is symmetric, i.e. no satellite drops are formed. For charged jets, (*b–d*), pinch-off is asymmetric. The satellite drops observed at breakup become progressively larger as N_E increases and exhibit large, bulbous cores.

along with the axial variation of the capillary pressure p_C (figure 22*b*) and axial velocity v evaluated along S_f (figure 22*c*). The first profile corresponds to the instant at which the proto-satellite is first observed, i.e. the point in time at which h_{min} shifts to an axial location $z = z_{min} < \pi/k$. At this instant, p_C increases monotonically from $z = 0$ to $z = \pi/k$, and v is everywhere negative, as is the case prior to the inception of the proto-satellite drop. As the jet thins in the vicinity of the new h_{min}, a maximum in the p_C that is located at some $z = z^* < \pi/k$ emerges in proximity to the new h_{min} owing to the increased local curvature of the free surface there. The second profile shows the first instant at which this maximum in the p_C is observed. Beyond this point, the direction of the capillary driving force in the proto-satellite drop is reversed, acting to slow but not reverse the flow of fluid into the swell, as can be seen in the third profile from a slightly later time. These profiles also show that, after the inception of the proto-satellite drop, h_{min} translates axially away from the initial neck as the jet deforms. This axial translation of h_{min}, like the inception of the proto-satellite drop, is driven by inertia and continues up to the point of pinch-off. At a given instant, while p_C is maximum at a point near h_{min}, the capillary pressure gradient and the radially averaged axial velocity are maximum at points downstream of h_{min}. When inertia is significant, as is the case in this example, the net efflux of fluid just downstream of h_{min} exceeds the net efflux of fluid in the immediate vicinity of h_{min}, resulting in what appears to be a smooth axial translation of h_{min} away from the initial neck as the jet evolves in time.

For uncharged jets in the Stokes flow regime, for which inertia is completely absent, both h_{min} and the maximum p_C remain at $z = \pi/k$ up to the point of pinch-off, and no satellite is formed (Papageorgiou 1995). However, this is not the case for charged Stokes jets, as figure 23 demonstrates. Here, jet profiles at the incipience of pinch-off from two-dimensional simulations are shown for (*a*) an uncharged jet ($N_E = 0$) and for charged jets with (*b*) $N_E = 1$, (*c*) $N_E = 3$ and (*d*) $N_E = 5$ in the Stokes flow limit. While no satellite drop is formed in the uncharged case, satellite drops are formed for charged Stokes jets, and the sizes of the satellite drops formed increase with N_E. The development of these satellites is driven not by inertia, but rather by a reversal of the direction of the gradient of the electrocapillary pressure $p_C + p_E$ in the vicinity of

$z = \pi/k$ that occurs during the temporal evolution of a jet. Initially, for small ε and $k'_{crit} < k < k_{crit}$, the electrocapillary pressure gradient along the jet drives a flow of fluid from the neck to the swell, causing the neck to thin. As the neck thins, the capillary pressure in the vicinity of $z = \pi/k$ increases owing to the increasing local curvature of the free surface, and the normal component of the Maxwell stress along the free surface, i.e. $-p_E$, in the vicinity of $z = \pi/k$ increases because of charge accumulation. These effects are observed immediately for $k'_{crit} < k < k_E$, in accord with linear theory, but are observed only after the neck has thinned significantly for $k_E < k < k_{crit}$. The peak in p_C about $z = \pi/k$ tends to be somewhat broader than the peak in p_E, as, to the leading order, p_C in that region varies roughly as $1/r$ while p_E varies roughly as N_E/r^2. The magnitudes of these peaks increase as the jet evolves in time, leading eventually to the emergence of a maximum in the electrocapillary pressure that is located at $z = z^* < \pi/k$ and consequently to the reversal of the electrocapillary pressure gradient within the jet. The reversal of the electrocapillary driving force in the portion of the neck between $z^* \leqslant z \leqslant \pi/k$ acts to reduce the efflux of fluid from the region, and consequently, at a slightly later time, a new h_{min} emerges at $z = z_{min} < \pi/k$, marking the inception of the proto-satellite drop. Shortly after the inception of the proto-satellite drop, a stagnation plane emerges upstream of the new h_{min}, above which the direction of flow is reversed. After this instant, the proto-satellite grows from an infusion of fluid from the proto-primary drop.

Figure 24 outlines the early stages of satellite drop development for a highly charged ($N_E = 5$) Stokes jet, showing a sequence of instants in the temporal evolution of the jet. Here, jet profiles for half a wavelength (figure 24*a*) are shown along with the axial variation of the electrocapillary pressure (figure 24*b*) and the axial velocity evaluated along S_f (figure 24*c*). For the first profile, $p_C + p_E$ increases monotonically from $z = 0$ to $z = \pi/k$, v is negative (i.e the flow is directed toward $z = 0$ all along the half-wavelength), and h_{min} is located at $z = \pi/k$. At the next time step (not shown), a maximum in $p_C + p_E$ emerges at $z = z^* < \pi/k$, though h_{min} remains located at $z = \pi/k$. The second profile shows the instant at which a new h_{min} emerges at $z = z_{min} < \pi/k$, marking the inception of the proto-satellite. Here, the reversal of the electrocapillary pressure gradient near $z = \pi/k$ is already pronounced, and the magnitude of the axial velocity near $z = \pi/k$ has decreased slightly. The third profile corresponds to the first instant in time at which there is a reversal in the flow field in the vicinity of $z = \pi/k$. The magnitude of the axial velocity has decreased considerably upstream of z^* relative to the previous profile. For the fourth profile shown, the stagnation plane just upstream of h_{min} and above which the direction of flow is reversed is clearly visible, and the satellite has begun to thicken around $z = \pi/k$, giving the first indications of the large bulbous satellite that will eventually separate from the primary drop (see figure 23*d*).

Figure 25 compares the evolution in time of the profile of and the flow field within an uncharged Stokes jet with that of a highly charged ($N_E = 5$) Stokes jet. The dashed horizontal lines indicate the axial location of h_{min} above $z = 0$, while the dot-dashed horizontal lines indicate the location of the interior stagnation plane above which the flow direction is reversed (i.e. flow is directed into the proto-satellite) in the region above $z = 0$. In the uncharged case, as mentioned above, the flow is directed continuously into the proto-primary drop (no satellite is formed in this case, making this designation somewhat arbitrary) throughout the temporal evolution of the jet, and h_{min} remains at its initial location ($z = \pi/k$) up to the point of pinch-off (see figure 23*a*). In the highly charged case, however, a proto-satellite drop has clearly developed prior to the point at which $h_{min} = 0.4$, along with a stagnation plane above

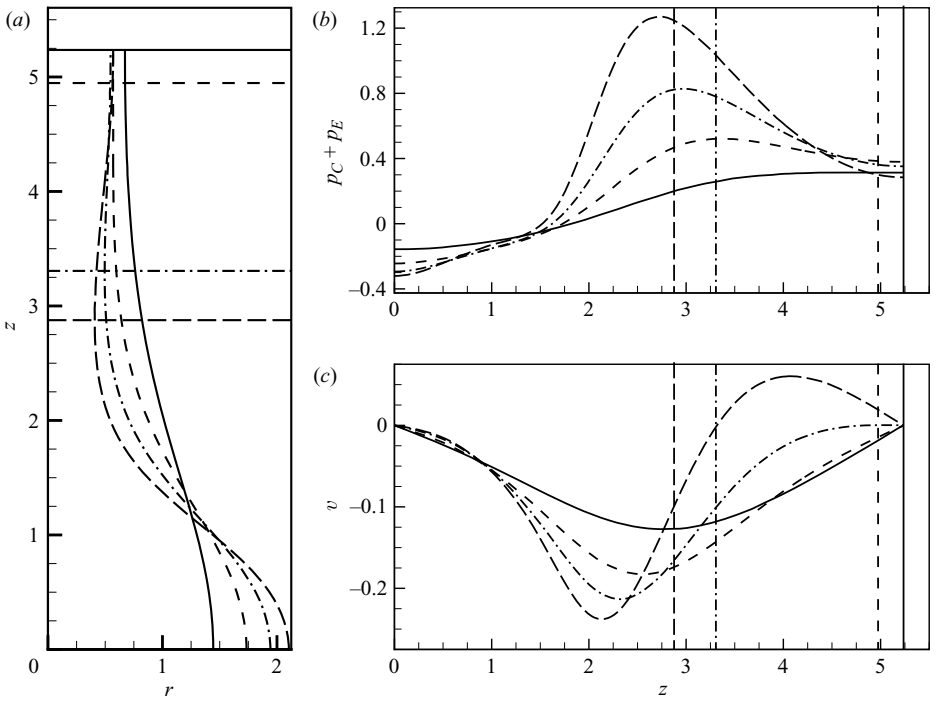

FIGURE 24. Influence of electrostatic stresses on satellite formation. Here, jet profiles, (*a*), are shown along with the axial variation of the electrocapillary pressure, (*b*), and axial velocity evaluated along S_f, (*c*), for a sequence of instants during the evolution in time of a highly charged ($N_E = 5$) jet in the Stokes flow limit subjected to a perturbation of wavenumber $k = 0.6$. The axial location of h_{min} at each instant is indicated by the horizontal lines in (*a*) and by the vertical lines in (*b*) and (*c*). Profiles are shown at instants corresponding to $h_{min} = 0.672$ (——), $h_{min} = 0.568$ (- - -), $h_{min} = 0.495$ (— · —) and $h_{min} = 0.408$ (– –).

which the direction of the flow is reversed. By the point at which $h_{min} = 0.2$, the proto-satellite drop has grown significantly at the expense of the proto-primary drop and has begun to take on the bulbous shape the satellite drop will have at pinch-off (see figure 23*d*).

For the case of charged Newtonian jets of low or moderate N_{Oh}, both of the mechanisms for satellite drop formation discussed above come into play, with the inertial mechanism being the more important of the two for slightly charged jets and the electrocapillary mechanism being more important for highly charged jets. Because the two mechanisms are complementary, however, it is not surprising that, for fixed N_{Oh} and k, satellite drop volumes are larger for charged jets than for uncharged jets. Figure 26 highlights the differences between the early stages of satellite formation for an uncharged ($N_E = 0$) moderately viscous jet of $N_{Oh} = 0.1$ and a highly charged ($N_E = 5$) jet of the same N_{Oh}. The transition from h_{min} being located at $z = \pi/k$ to h_{min} being located at $z = z_{min} < \pi/k$ occurs much earlier for the highly charged jet ($h_{min} = 0.826$) than for the uncharged jet ($h_{min} = 0.408$). This is due to an early reversal of the sign of the electrocapillary pressure gradient in the neck in the highly charged case, as was the case with the highly charged Stokes jet described above. Shortly after the transition from h_{min} being located at $z = \pi/k$ to h_{min} being located at $z = z_{min} < \pi/k$ ($h_{min} = 0.734$), an interior stagnation plane, indicated by the dot-dashed horizontal line, emerges in the highly charged jet upstream of h_{min}. Above the

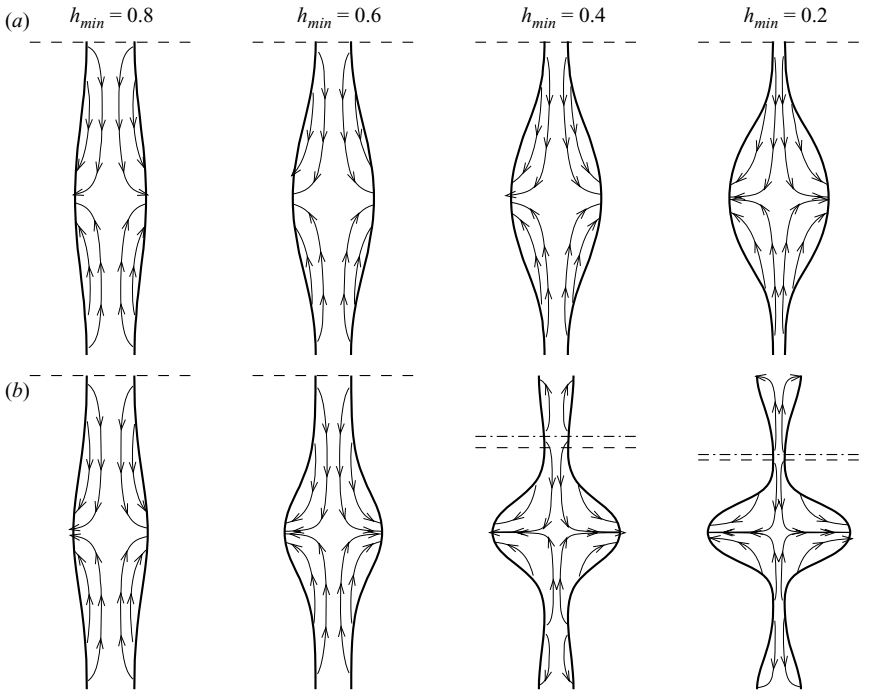

FIGURE 25. Influence of electrostatic stresses on satellite formation. Jet profiles and streamlines are shown for both (*a*) uncharged ($N_E = 0$) and (*b*) charged ($N_E = 5$) jets in the Stokes flow limit. The uncharged and charged jet profiles are compared at equivalent h_{min}. The location of the interior stagnation plane (upper half) is included for reference ($- \cdot -$) when applicable, along with the location of h_{min} ($- - -$). Here, $k = 0.6$.

stagnation plane, fluid flows toward $z = \pi/k$, whereas below the stagnation plane fluid flows toward $z = 0$. This stagnation plane moves steadily away from $z = \pi/k$ as the jet evolves toward breakup, trailing h_{min}, so that fluid is continually pumped away from the portion of the jet that will form the primary drop into the satellite. This results in the development of a much larger satellite in the highly charged case than in the uncharged case, for which no such stagnation plane develops until much later in the evolution of the jet ($h_{min} \approx 0.029$, not shown).

3.4.4. *Electrostatic stresses and primary drop formation*

While primary drops formed at pinch-off from charged jets are smaller than their counterparts formed from uncharged jets, figures 9 to 12 show that primary drops formed from charged jets are also more oblate or radially elongated than are those formed from uncharged jets. This effect is more pronounced at higher N_E and is observed for the entire range of wavenumbers and Ohnesorge numbers examined in this work. This effect is not too surprising in light of the nature of the electrocapillary driving force along the surface of the swell in the early stages of the temporal evolution of a charged jet. Driven by the electrocapillary pressure gradient along the free surface of a charged jet, fluid flows from the neck into the swell, causing the jet to expand radially in the vicinity of $z = 0$. This process leads eventually to the formation of a large primary drop centred at $z = 0$, as is the case with uncharged jets. For charged jets, however, as the swell expands, charge begins to accumulate preferentially along the portion of the free surface in the vicinity of

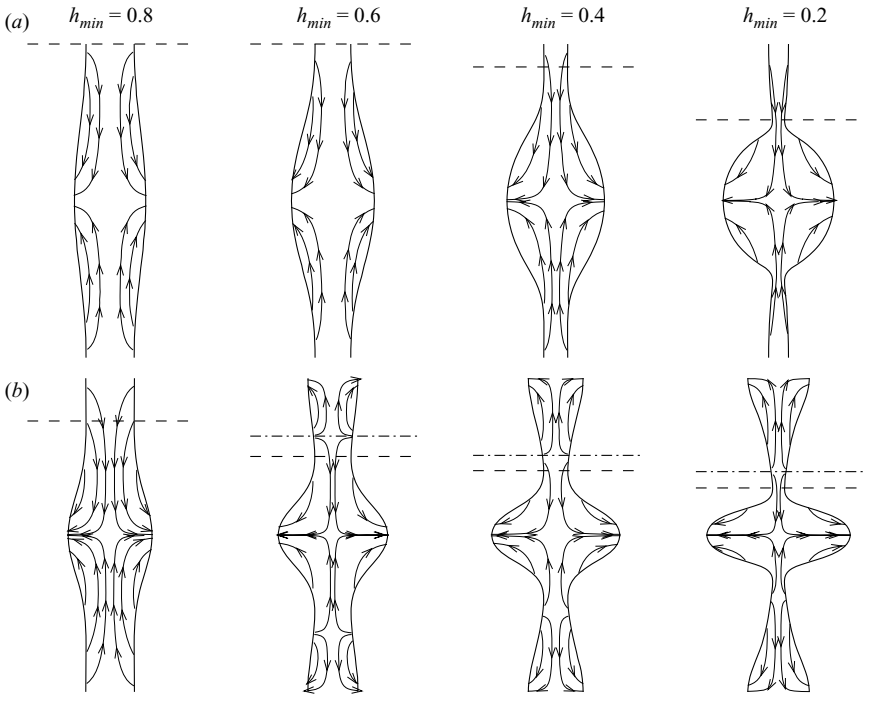

FIGURE 26. Same as figure 25 except for moderately viscous jets of $N_{Oh} = 0.1$.

$z = 0$ (i.e. where the drop is most elongated), just as charge accumulates preferentially at the peaks of planar waves. The accumulation of charge around $z = 0$ increases the magnitude of the local electrocapillary pressure gradient, which acts to enhance the rate of flow of fluid into the region. This results in enhanced radial elongation of the jet near $z = 0$ with an attendant increase in the local surface charge density. Figure 27 highlights the differences in the early development of primary drops between uncharged and charged jets described above. Jet profiles (top) obtained from two-dimensional simulations, along with the axial variation of the surface charge density q (middle) and electrocapillary pressure (bottom) are shown for an uncharged jet (figure 27*a*) and a highly charged jet ($N_E = 5$) (figure 27*b*) at several instants in time during their temporal evolution. Here, the wavenumber is chosen such that $k = 0.6 \approx k_E$ to demonstrate that the phenomenon described above is nonlinear in nature. There is little discernible difference between the uncharged jet profile and the charged jet profile when $h_{min} = 0.9$, and q in the charged case is nearly uniform at that instant, as is expected from linear theory. As the charged jet continues to deform, charge begins to accumulate preferentially in the vicinity of $z = 0$, as described above. This alters the local electrocapillary pressure gradient in such a way as to increase the flow of fluid into that region, resulting in increased radial elongation. When $h_{min} = 0.85$, a noticeable peak has developed in the surface charge density centred about $z = 0$ in the charged case, and the jet profile in the charged case is slightly more radially elongated in the vicinity of $z = 0$ than is the case with the corresponding uncharged jet profile. These effects become quite pronounced as the charged jet continues to deform, so that the jet is visibly more radially elongated in the vicinity of $z = 0$ in the charged case than is the case for the the uncharged jet when $h_{min} = 0.8$. Here, the axial variation of the electrocapillary pressure is clearly larger near $z = 0$

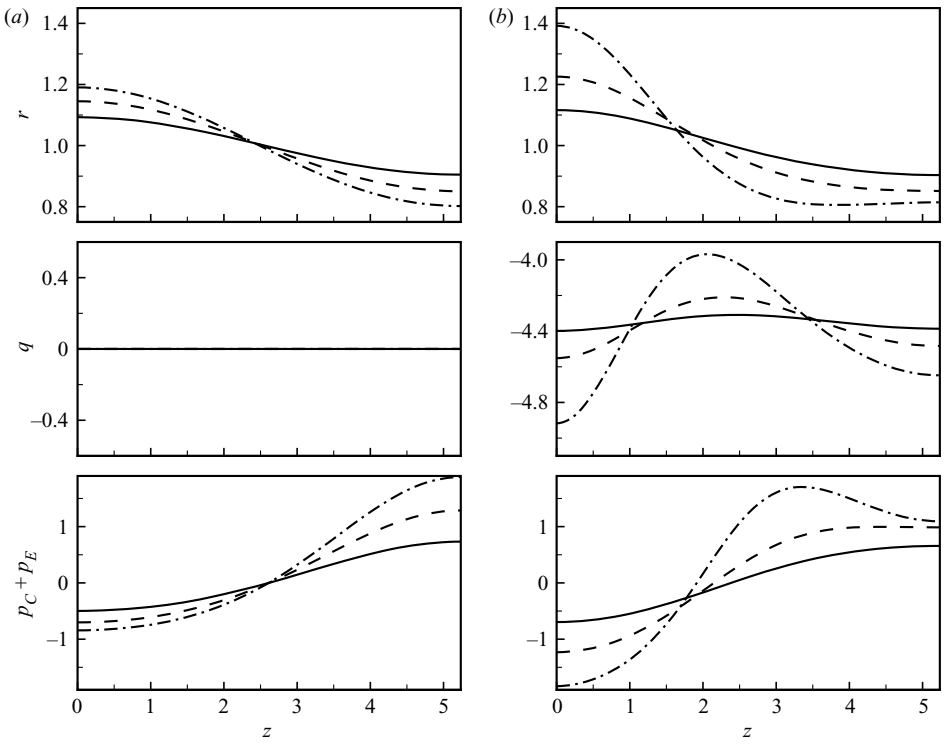

FIGURE 27. Influence of electrostatic stresses on the early development of primary drops. Here, jet profiles (top) from two-dimensional simulations, along with surface charge density q (middle) and electrocapillary pressure $p_C + p_E$ (bottom) variations along S_f, are shown for, (a), an uncharged ($N_E = 0$) jet and, (b), a highly charged ($N_E = 5$) jet at instants corresponding to $h_{min} = 0.9$ (——), $h_{min} = 0.85$ (- - -), and $h_{min} = 0.8$ (— · —). For both (a) and (b), the jets are moderately viscous ($N_{Oh} = 0.1$) and $k = 0.6 \approx k_E$. Note that the jet profiles shown are not to scale in order to facilitate comparison of the uncharged and highly charged cases. For further ease of comparison, the electrocapillary pressure of the unperturbed filament (i.e. $N_{Oh}^{-1}(1 - N_E/\log^2(R))$) has been subtracted from the computed electrocapillary pressure in each case.

in the charged case, indicating that the jet will continue to elongate radially in that region to a greater extent than in the uncharged case. Ultimately, this process results in the formation of primary drops which are considerably more oblate than those formed from uncharged jets.

The formation of oblate primary drops from charged jets, as mentioned previously, has been observed both when $k > k_E$ and when $k < k_E$. With regard to linear theory, this may seem counterintuitive, since while for an infinitesimal amplitude perturbation with $k > k_E$ the surface charge density is maximum at $z = 0$, for $k < k_E$ the surface charge density is actually minimum at $z = 0$. However, as alluded to previously, the formation of more oblate primary drops from charged jets is an entirely nonlinear effect. Figure 28 shows an example of the early stages of the temporal evolution of two highly charged ($N_E = 5$), moderately viscous jets of $N_{Oh} = 0.1$ subjected to perturbations of wavenumbers $k = 0.7$ and 0.4. Jet profiles (top) are shown along with the axial variation of the surface charge density (middle) and electrocapillary pressure (bottom) along the free surface at several instants in time during the early stages of their temporal evolution. In the earliest stages of jet deformation, the

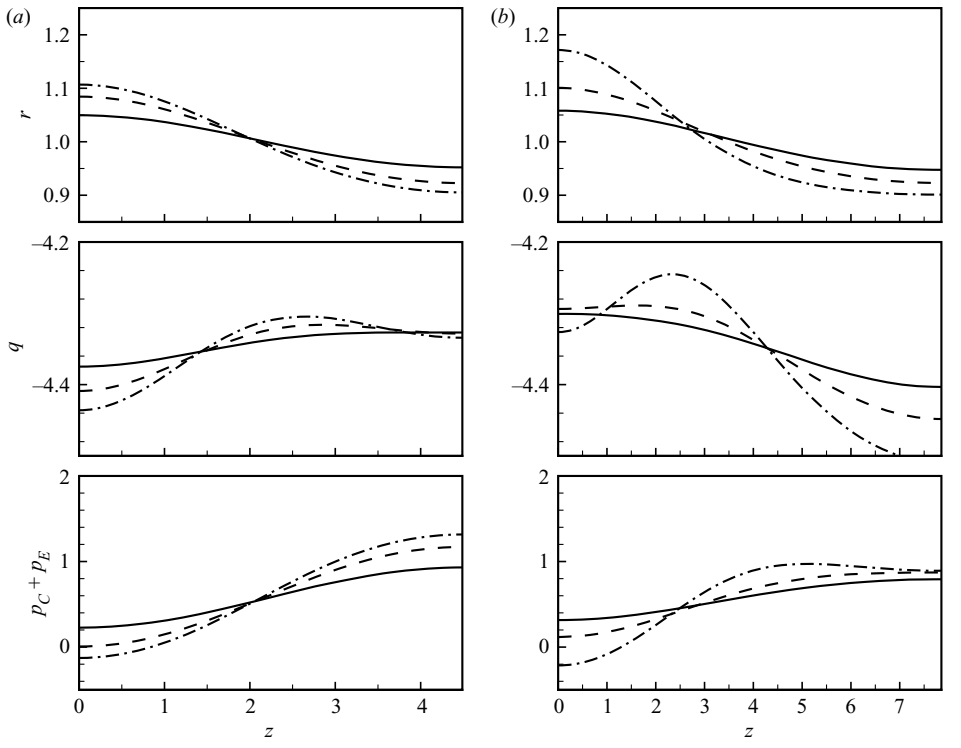

FIGURE 28. Influence of electrostatic stresses on the early development of primary drops. Here, jet profiles (top) for highly charged ($N_E = 5$), moderately viscous ($N_{Oh} = 0.1$) jets subjected to perturbations of wavenumbers (*a*) $k = 0.7$ and (*b*) $k = 0.4$ are shown at instants corresponding to $h_{min} = 0.95$ (——), $h_{min} = 0.925$ (- - -), and $h_{min} = 0.9$ (— · —). Note that here the jet profiles are not shown to scale. The surface charge density q (middle) and electrocapillary pressure $p_C + p_E$ (bottom) along S_f are also shown.

surface charge density varies along the free surface in a manner consistent with linear theory in both cases. For the relatively short wave ($k = 0.7 > k_E$), the magnitude of the surface charge density decreases monotonically along S_f when $h_{min} = 0.95$, with its maximum (minimum) located at $z = 0$ ($z = \pi/k$), while for the longer wave ($k = 0.4 < k_E$), the surface charge density increases monotonically along S_f, with its minimum (maximum) at $z = 0$ ($z = \pi/k$). As the jets continue to deform, the maximum magnitude of the surface charge density remains located at $z = 0$ for the shorter wave, though the sharpness of the peak around $z = 0$ increases as the jet elongates radially in that region. For the longer wave, the local variation of q around $z = 0$ begins to flatten out as the jet deforms, as is apparent from the profile shown when $h_{min} = 0.925$. Here, while electrocapillary stresses have slowed the flow of fluid from the neck into the swell, the overall electrocapillary driving force has still caused the swell to expand radially, acting to increase the local surface charge density around $z = 0$. As the portion of the jet around $z = 0$ continues to expand under the action of the electrocapillary pressure gradient, a peak in the surface charge density eventually develops centred about $z = 0$. This peak is clearly visible when $h_{min} = 0.9$. Once this peak has developed, the local electrocapillary pressure gradient acts to accelerate the radial elongation of this region in the manner described above. In both cases, then, as the swell expands, the surface charge density around $z = 0$ evolves in such a way as to promote radial

elongation of the jet in that region, leading ultimately to the formation of oblate primary drops.

In their study of inviscid, highly charged jets, Setiawan & Heister (1997) report that primary drops formed from charged jets are more 'squashed' or oblate than those formed from uncharged jets, as has been demonstrated in this work for Newtonian fluids of arbitrary viscosity. At very high charge levels ($N_E/\log^2(R) > 1-2$), however, these authors propose a different mechanism of breakup, postulating that a 'tiny ring of fluid at the tip of the peak' is sheared off from the peak of the swell as it elongates radially into the electric field. Their claim is based on the behaviour of the free-surface nodes in their boundary-element simulations at, and immediately adjacent to, the radial peak of the swell (i.e. at $z = 0$ in the coordinate frame used in the present work). According to these authors, as the swell elongates radially, expanding rapidly under the action of the strong electrocapillary pressure gradient there, a point is reached beyond which, while the node at the radial peak of the swell has a large positive radial velocity, the two neighbouring nodes have large negative radial velocities. Results are shown for jets subjected to very short wave perturbations ($k = 1.3$), and the phenomena described is observed for $N_E = 7.5$ and larger with $R = 10$. Although the phenomena described by Setiawan & Heister (unphysical behaviour of adjacent nodes) is most probably an artefact of insufficient mesh refinement, the nature of the electrostatic stresses acting at the periphery of a proto-primary drop at high levels of electrification do lend some credence to the idea that the mechanism of breakup may be altered at very high charge levels. This idea is explored in the following subsection.

3.4.5. *Drop formation at very high N_E*

In this subsection, the breakup of electrified jets at very high electric Bond numbers is examined using the two-dimensional algorithm. To resolve the temporal evolution of the primary drop in fine detail, the mesh designated Mesh II, as described in Appendix B.1, is used. Slightly viscous (N_{Oh}) jets subjected to very short wavelength perturbations ($k = 1.3$) are examined to allow for comparison with the inviscid analysis of Setiawan & Heister. The one-dimensional algorithm is not suitable for this analysis, as for even moderately high N_E the one-dimensional algorithm fails prior to pinch-off for slightly viscous jets.

Figure 29 shows a sequence of instants in time in the temporal evolution of slightly viscous jets at three high values of N_E. Profiles corresponding to $h_{min} = 0.5$ (relatively early in the temporal evolution of a jet toward pinch-off) show the higher N_E is, the more oblate are the proto-primary drops. Further, the proto-primary drop at $N_E = 7.5$ has a more spiked appearance than the proto-primary drops at the lower N_E. Radial elongation of the proto-primary drops continues as breakup is approached, as can be seen from the profiles corresponding to $h_{min} = 0.1$. For $N_E = 5.5$, the roughly oblate spheroidal proto-primary drop shape characteristic of jet breakup at low to moderately high N_E is observed at this point, but for $N_E = 7.5$, the shape of the proto-primary drop resembles a flattened disk bulging in the centre. Moreover, a substantial ring-like structure appears to be forming at the periphery of the disk (see below). The primary drops formed at pinch-off ($h_{min} = 0.002$), while exhibiting the interface overturning characteristic of pinch-off for slightly viscous jets, differ little at the periphery from the profiles corresponding to $h_{min} = 0.1$, as the dynamics at the pinch-point occur on a much faster time scale than the dynamics at the periphery. However, it is clear that the dynamics at the periphery are accelerated at very high N_E.

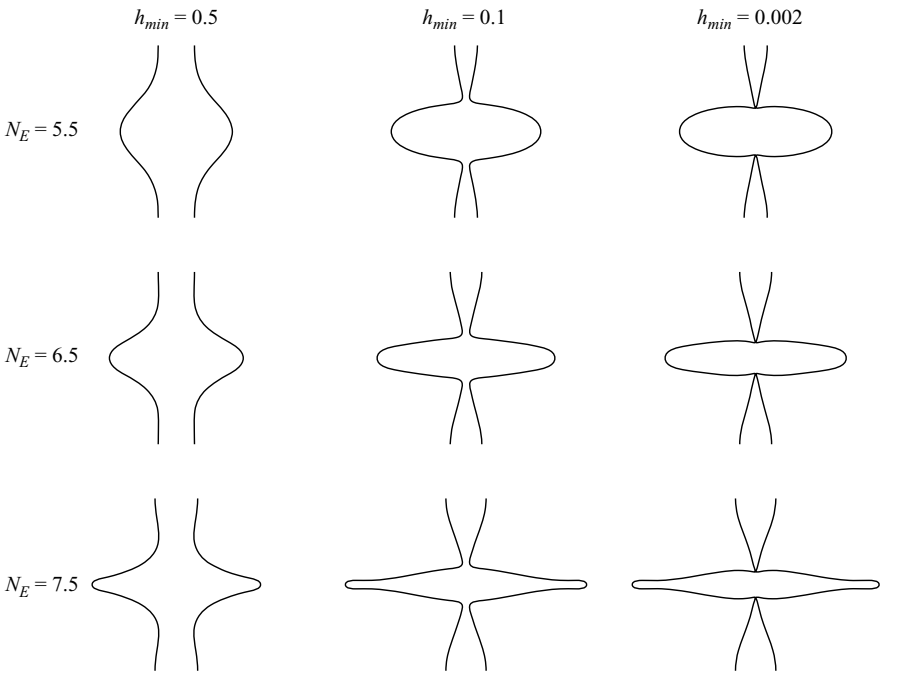

FIGURE 29. Temporal evolution of jet profiles at very high N_E. A series of jet profiles are shown for slightly viscous jets of $N_{Oh} = 0.01$ subjected to very short wavelength perturbations ($k = 1.3$) at very high N_E. Jet profiles are compared at instants in time when $h_{min} = 0.5$, $h_{min} = 0.1$ and at pinch-off ($h_{min} = 0.002$) for jets with $N_E = 5.5$, $N_E = 6.5$ and $N_E = 7.5$.

Figure 30 shows in detail the peripheral region of the primary drop formed at pinch-off for $N_E = 7.5$. The streamlines shown indicate that the flow is nearly radial in this region. Further, radial velocity contours indicate that the radial velocity is maximum at a point upstream of the extreme periphery of the primary drop. In the vicinity of the location of the maximum radial velocity, the thickness of the disk-like structure of the primary drop exhibits a local minimum (i.e. the free surface in this region cannot be described by a single-valued function of the axial coordinate). Prior to pinch-off, there is a net efflux of fluid from the vicinity of this minimum into the extreme periphery of the primary drop, resulting in the formation of this ring-like structure. These structures are not observed for $N_E < 7$ for the parameters examined here. Although it is not possible with the present algorithm to continue simulations past the point of pinch-off, the trends observed prior to pinch-off indicate that this ring-like structure will continue to grow after breakup and may eventually detach from the bulk of the primary drop.

Figure 31 shows how the charge ratios $(Q/Q_R)_{main}$ and $(Q/Q_R)_{sat}$ for the primary and satellite drops formed at pinch-off vary with N_E for slightly viscous jets of $N_{Oh} = 0.01$ subjected to very short wavelength perturbations ($k = 1.3$) at moderately high to very high electric Bond numbers. $(Q/Q_R)_{sat}$, which increases with increasing N_E in the low to moderately high N_E range, exhibits a maximum and drops off at very high N_E; this drop off is most probably due to increased effective shielding of satellite drops from the electric field owing to the proximity of the far more radially elongated primary drops that form at these N_E. For low to moderately high electric Bond numbers, $(Q/Q_R)_{main}$ increases monotonically with N_E, as described

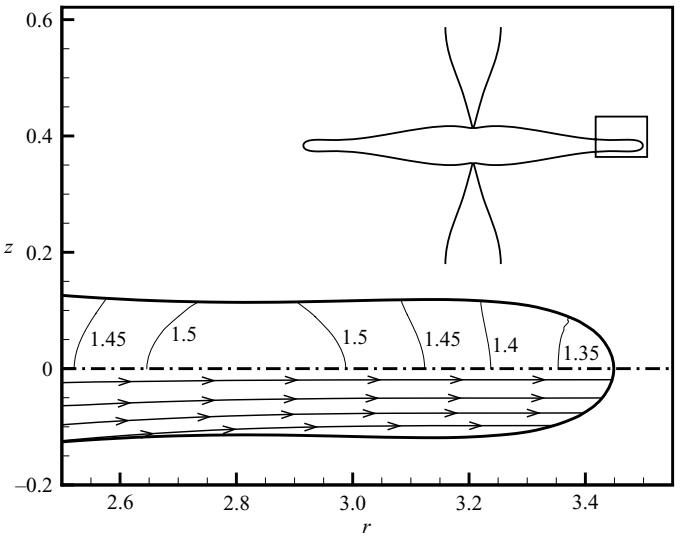

FIGURE 30. Electrohydrodynamics at the periphery of a primary drop at pinch-off at very high electric Bond numbers. Here, the peripheral portion of the primary drop formed at pinch-off from a slightly viscous jet of $N_{Oh} = 0.01$ subjected to a very short wavelength perturbation ($k = 1.3$) is shown in detail for $N_E = 7.5$. The full jet profile is indicated as an insert, and the box shows the extent of the region shown in the main figure. Also shown in the main figure are the radial velocity contours (upper portion) and streamlines (lower portion).

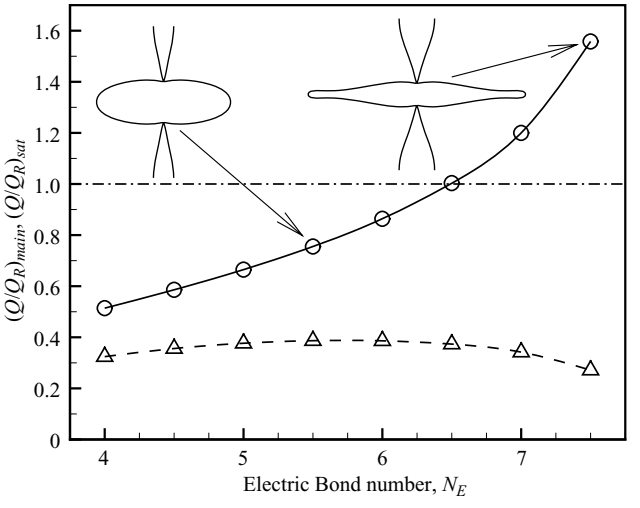

FIGURE 31. Drop charges at very high electric Bond numbers. Here, the ratio of the drop charge Q to the Rayleigh charge limit ($Q_R = \sqrt{96\pi N_E V}$) for primary (——) and satellite (- - -) drops formed at pinch-off ($(Q/Q_R)_{main}$ and $(Q/Q_R)_{sat}$, respectively) are shown for moderately high to very high N_E. Results are shown for slightly viscous jets of $N_{Oh} = 0.01$ subjected to very short wavelength perturbations ($k = 1.3$). Also shown as inserts are jet profiles for $N_E = 5.5$ and $N_E = 7.5$.

in § 3.4.2, though in that range, the primary drops are Coulombically stable (i.e. $(Q/Q_R)_{main} < 1$ in this range). $(Q/Q_R)_{main}$ continues to increase with N_E at very high N_E, and for the parameter set examined here, the primary drops formed at pinch-off become Coulombically unstable when N_E exceeds 6.5. This transition corresponds

closely with the morphological transition described above: for $N_E < 6.5$, primary drops have a roughly oblate spheroidal shape, whereas for $N_E > 6.5$, primary drops exhibit a flattened disk-like structure with a central bulge. The structures observed at very high N_E in this work, however, are most probably unphysical, as these shapes may be unstable with respect to non-axisymmetric perturbations. To our knowledge, no experimental evidence has been reported for the development of the ring-like structures observed in figure 29. Cloupeau & Prunet-Foch (1989) indicate rather that for very highly charged jets, the drops formed at pinch-off emit fine jets from their peripheries when their surface charges exceed the Rayleigh limit. Alternately, these authors report that either kink instabilities or the emission of multiple fine jets from the periphery of the original jet can occur in lieu of axisymmetric pinch-off. These types of instabilities cannot, of course, be observed with the algorithms used in this work owing to the assumptions of axisymmetry employed here.

It should be noted that Setiawan & Heister (1997) report that the boundary-element code used in their inviscid analysis fails well before pinch-off ($h_{min} \approx 0.65$) for the same set parameter of ($k = 1.3$, $N_E = 7.5$, $R = 10$) shown in figure 29.

3.5. *Electrostatic stresses and interface overturning*

In the absence of electrostatic stresses, interface overturning has been observed computationally in studies of capillary pinch-off in the inviscid limit by numerous authors (Mansour & Lundgren 1990; Chen & Steen 1997; Day *et al.* 1998). Day *et al.* have shown through boundary-element simulations that, for an inviscid liquid drop breaking in air, the local interface near the pinch point evolves in a self-similar manner, adopting angles of 18.1° and 112.8° measured from the axis through the liquid for the satellite and primary drops, respectively. This result is independent of the ICs. As the latter angle is greater than 90°, the interface is deemed to be overturned (i.e. the interface cannot be described by a single-valued function of the axial coordinate). Wilkes *et al.* (1999) first demonstrated that interface overturning can occur with Newtonian fluids at low N_{Oh} in their computational study of drop formation from a tube. Chen *et al.* (2002), using a G/FEM algorithm, also report interface overturning with Newtonian fluids at low N_{Oh} and compare their results to experiments, demonstrating excellent agreement. Overturning of the interface of a primary drop is thought to be due to inefficient transport of axial momentum. As pinch-off is approached, a high-velocity stream concentrated around the axis of the jet is pumped into the primary drop from the rapidly thinning neck owing to the high capillary pressure there. For slightly viscous fluids, the axial momentum associated with this stream cannot be efficiently transmitted into the bulk of the primary drop through the action of viscous shear stresses, and so remains concentrated around the axis. The inertia of this stream, then, acts essentially to drag the local interface into the primary drop, resulting in interface overturning.

The influence of electrostatic stresses on interface overturning with charged jets has not been examined to date. The slender-jet algorithm used by López-Herrera *et al.* (1999) and López-Herrera & Gañan-Cálvo (2004) and also the one-dimensional algorithm used here artificially prohibit interface overturning by requiring that the interface be a single-valued function of z. Setiawan & Heister (1997), in their inviscid analysis, did not resolve the pinch region in sufficient detail to observe substantial interface overturning.

Two-dimensional simulations show that interface overturning occurs for both uncharged and charged jets at low to moderate values of N_{Oh}, as can be seen from the computed jet profiles at pinch-off shown in figures 9–11 and 17. Interface

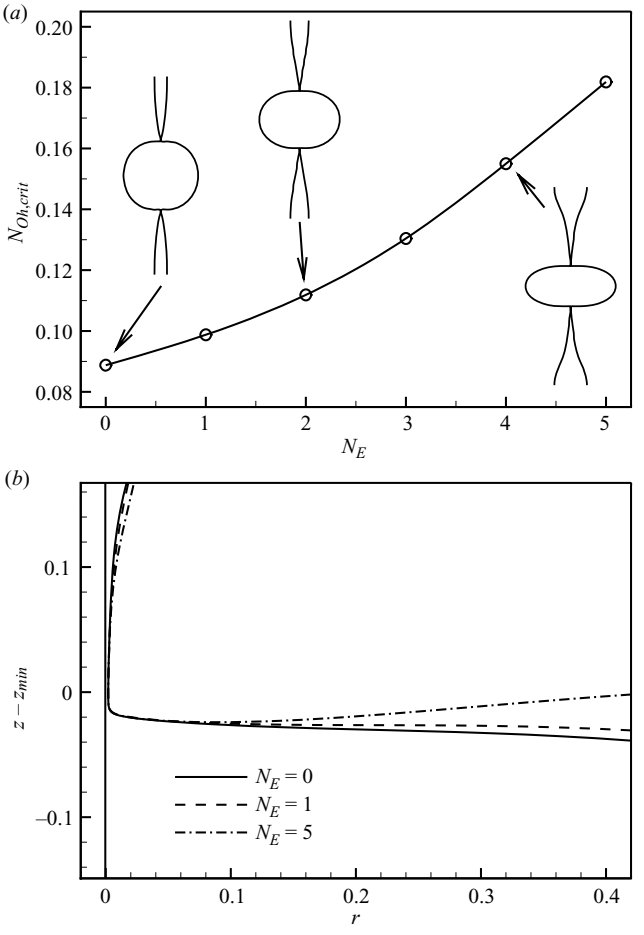

FIGURE 32. Influence of N_E on interface overturning for jets subjected to perturbations of wavenumber $k = 0.6$. (*a*) The critical Ohnesorge number $N_{Oh,crit}$ below which interface overturning occurs as a function of N_E. Also shown as inserts are jet profiles near pinch-off. (*b*) Interface profiles for moderately viscous filaments of $N_{Oh} = 0.1$ near pinch-off ($h_{min} = 0.002$) at various N_E. While the interface does not overturn with no applied electric field, $N_E = 0$, overturning of the interface is pronounced for the highly charged case, $N_E = 5$.

overturning is observed for cases in which the Ohnesorge number is less than a critical value, $N_{Oh,crit}$, which depends on N_E and to a lesser extent on k. The variation of $N_{Oh,crit}$ with N_E for $k = 0.6$ is shown in figure 32(*a*), along with computed jet profiles at selected values of $N_{Oh,crit}$. By computing curves like that shown in figure 32(*a*) at other wavenumbers, it is possible to construct a phase diagram for the occurrence of interface overturning with charged jets in (N_E, k, N_{Oh}) space. Figure 32(*a*) indicates that electrostatic stresses act to promote interface overturning, as $N_{Oh,crit}$ increases monotonically with N_E. Similar trends have been observed for all wavenumbers examined in this work.

Figure 32(*b*) shows portions of computed jet profiles from two-dimensional simulations at the incipience of pinch-off for moderately viscous jets of $N_{Oh} = 0.1$ for several values of N_E. For ease of comparison, the profiles are shifted so that the minimum radius h_{min} has the same axial location $z - z_{min}$ for each profile. The

influence of electrostatic stresses on interface overturning is clearly demonstrated here. In the uncharged case for this combination of k and N_{Oh}, interface overturning is not observed ($N_{Oh,crit} \approx 0.089$ for uncharged jets at this wavenumber). For charged jets, although interface overturning is not observed at low N_E, the interface of the primary drop near the pinch region steepens as N_E is increased. The interface of the primary drop near the pinch region in the computed jet profile shown for $N_E = 1$, although not overturned, is nearly horizontal. Interface overturning is first observed for charged jets at this combination of k and N_{Oh} when $N_E \approx 1.13$ (not shown), the point corresponding to $N_{Oh,crit} = 0.1$ in figure 32(a). At higher N_E, interface overturning becomes visibly more pronounced, as can be seen from the computed jet profile shown for $N_E = 5$.

3.6. *Electrostatic stresses and the local dynamics of pinch-off*

In this section, the influence of an applied electric field on the local dynamics of pinch-off is examined. While other system parameters, and particularly the electric Bond number, play a role here, the extent to which an applied electric field influences pinch-off dynamics depends to a large degree on the Ohnesorge number. To demonstrate this, it is worth first examining how the surface charge density in the pinch region evolves as breakup is approached. Figure 33 shows computed jet profiles at times approaching pinch-off for a range of moderately viscous charged jets. The axial variation of the surface charge density q is shown, along with the shape profiles in each case. The results shown are from two-dimensional simulations using Mesh I with $N_{z1} = 500$ (see Appendix B.1). For each profile shown, the axial location of the minimum radius along the free surface h_{min} (i.e. the pinch point) is indicated by the horizontal lines. For each N_{Oh}, jet profiles are shown at sequential instants in time approaching pinch-off, corresponding to $h_{min} = 0.004$ and $h_{min} = 0.002$. At low N_{Oh}, the pinch region is almost totally shielded from the applied electric field by the overturned interface of the primary drop, and the surface charge density q there falls nearly to zero. The profiles shown in figures 33(a) and 33(b) demonstrate this effect for $N_{Oh} = 0.1$. Thus, when $N_{Oh} = 0.1$, q in the vicinity of h_{min} increases little from the instant at which $h_{min} = 0.004$ to that at which $h_{min} = 0.002$. As N_{Oh} is increased, the extent of interface overturning diminishes, and the pinch region is more exposed to the applied electric field. For $N_{Oh} = 0.178$, which is very close to $N_{Oh,crit}$ for this combination of N_E and k (see § 3.5), while q is still relatively small in the vicinity of the pinch point, figures 33(c) and 33(d) show a noticeable increase in q from the instant at which $h_{min} = 0.004$ to that at which $h_{min} = 0.002$. Here, the development of a peak in q upstream of h_{min} that increases steadily in magnitude as pinch-off is approached, corresponding to the thinning of the thread-like filament connecting the primary and satellite drops, is observed. The magnitude of this peak drops off sharply near the primary drop as a consequence of increased shielding of the filament from the electric field provided by the proximity of the primary drop. The length of this thread-like filament increases substantially with N_{Oh}, and the size of this peak increases accordingly, as can be seen from the profiles for $N_{Oh} = 0.316$ (figures 33e, f). The increase in the local surface charge density in the pinch region at fixed h_{min} with N_{Oh} is largely due to the location of the pinch point. For both uncharged and charged jets, the distance between the pinch point and the leading edge of the primary drop increases with N_{Oh}, and consequently the effectiveness of the shielding of the pinch region from the electric field provided by the proximity of the primary drop diminishes as N_{Oh} is increased.

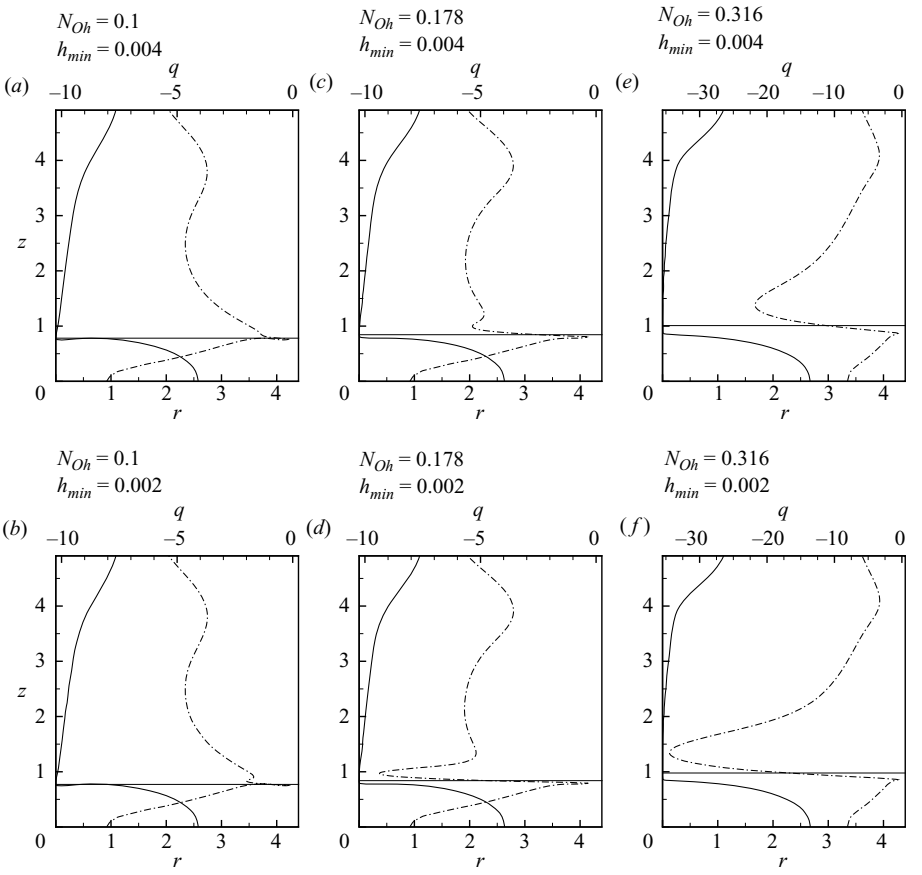

FIGURE 33. Surface charge density at the incipience of pinch-off. Here, computed jet profiles (——) and surface charge densities q (- · -) obtained from two-dimensional simulations are shown for highly charged ($N_E = 5$), moderately viscous jets ($0.1 \leqslant N_{Oh} \leqslant 0.316$) subjected to perturbations of wavenumber $k = 0.6$. The horizontal lines indicate the axial location of the minimum radius h_{min}.

Figure 33 suggests that the applied electric field should not influence the dynamics of pinch-off in any significant way at low Ohnesorge numbers, as the pinch region is almost totally shielded from the field by the overturned interface of the primary drop. However, because the surface charge density in the pinch region increases dramatically as pinch-off is approached at higher N_{Oh}, the applied electric field may have a drastic effect on pinch-off dynamics. Recall that the electrostatic pressure is related to the surface charge density by $p_E = -(1/4)N_{Oh}^{-1}N_E^{-1}q^2$. For the electric field to have a significant influence on pinch-off dynamics, the magnitude of the electrostatic pressure must be comparable to the capillary pressure. Figure 34 shows how the absolute value of the ratio of the electrostatic pressure to the capillary pressure $-p_E/p_C$ evaluated at h_{min} varies with h_{min} as pinch-off is approached for highly charged ($N_E = 5$) jets at various N_{Oh} and also in the Stokes flow limit. The results shown are from two-dimensional simulations using Mesh I, with $N_{z1} = 500$. For moderately viscous jets ($N_{Oh} = 0.1$), $-p_E/p_C$ drops off rapidly as pinch-off is approached. For example, at $h_{min} = 0.002$, p_C is more than four orders of magnitude larger than $-p_E$. Qualitatively similar behaviour is exhibited by jets at lower N_{Oh} (not

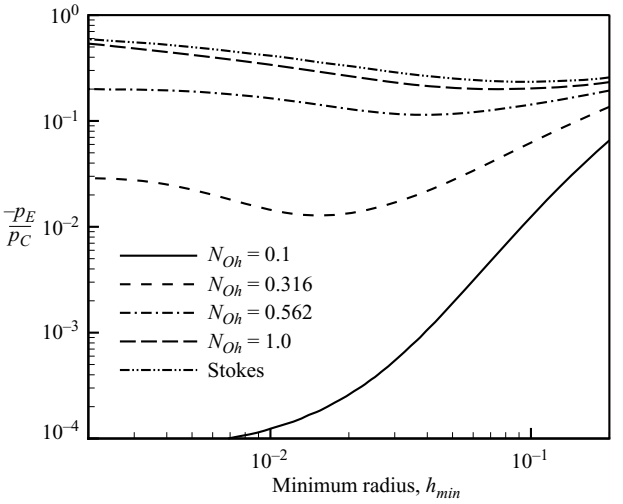

FIGURE 34. Balance of electrostatic and capillary stresses as pinch-off is approached. Here, the ratio of electrostatic stress to the capillary stress evaluated at h_{min} as pinch-off is approached is shown for a range of N_{Oh} and also for the Stokes flow limit. Results shown are for highly charged jets ($N_E = 5$) that have been obtained from two-dimensional simulations. Here, $k = 0.6$. While electrostatic stresses are dwarfed by capillary stresses at low to moderate N_{Oh}, electrostatic stresses and capillary stresses are comparable at higher N_{Oh} and in the Stokes flow limit, suggesting that the local pinch-off dynamics are relatively unaffected by electrostatic stresses at low N_{Oh} but are significantly influenced by electrostatic stresses at high N_{Oh}.

shown), for which $-p_E/p_C$ drops off even more rapidly as pinch-off is approached. These results strongly suggest that an applied electric field does not influence the local pinch-off dynamics at low Ohnesorge numbers, even at high N_E. The situation is different in the Stokes flow limit. Here, $-p_E/p_C$ increases steadily as pinch-off is approached. For example, at $h_{min} = 0.002$, $-p_E$ is nearly as large as p_C. Similar trends are observed with Newtonian jets at large Ohnesorge numbers, as may be seen from the curve corresponding to $N_{Oh} = 1$. From these results, it is clear that at large N_{Oh}, electrostatic stresses will have a significant impact on the local pinch-off dynamics of charged jets. Whether or not an applied electric field will significantly impact pinch-off at intermediate Ohnesorge numbers ($0.1 < N_{Oh} < 1$) is more difficult to determine, as it depends in large degree on the electric Bond number. In this range, $-p_E/p_C$ depends very strongly on N_{Oh}, as the curves shown for $N_{Oh} = 0.316$ and $N_{Oh} = 0.562$ demonstrate. It should be noted that López-Herrera & Gañan-Cálvo (2004), in their analysis of electrified jet breakup with a slender-jet algorithm, make a similar claim for pinch-off dynamics of charged jets being relatively unaffected by an applied electric field at low to moderate N_{Oh}, though the results shown in that work are for considerably lower N_E.

A series of two-dimensional simulations and corresponding one-dimensional simulations comparing the relative importance of electrostatic and capillary stresses in the pinch region as $h_{min} \to 0$ have been conducted to determine how accurately the one-dimensional algorithm predicts the influence of electrostatic stresses on pinch-off dynamics. Figure 35 compares results from the two algorithms for highly charged ($N_E = 5$) jets at $N_{Oh} = 0.1$ and $N_{Oh} = 1$. As with figure 34, figure 35 shows the variation of the ratio $-p_E/p_C$ evaluated at h_{min} with h_{min} as pinch-off is approached. Figure 35 shows that, for both moderately viscous and viscous jets, the one-dimensional

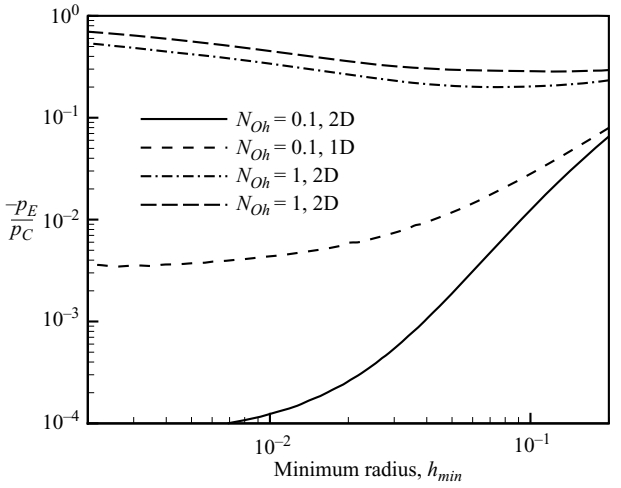

FIGURE 35. Comparison of the ratio of electrostatic stress to the capillary stress evaluated at h_{min} as pinch-off is approached computed from two-dimensional simulations with that computed from one-dimensional simulations. The results shown are for highly charged ($N_E = 5$) jets of $N_{Oh} = 0.1$ and $N_{Oh} = 1$. Here, $k = 0.6$. Note that the one-dimensional algorithm consistently overestimates the magnitude of the electrostatic stress relative to the capillary stress in the pinch region in both cases.

algorithm significantly overestimates the relative importance of electrostatic stresses on the pinch region as $h_{min} \to 0$ relative to the predictions of the two-dimensional algorithm. At $h_{min} = 0.002$, the stress ratio predicted by the one-dimensional algorithm for $N_{Oh} = 0.1$ is nearly two orders of magnitude larger than that predicted by the two-dimensional algorithm. Here, and at lower N_{Oh}, this deviation can be attributed in large part to the failure of the one-dimensional algorithm to predict interface overturning. The near total shielding of the pinch region from the applied electric field provided by the overturned interface of the primary drop at low N_{Oh}, observed in two-dimensional simulations, is not predicted by the one-dimensional algorithm, and accordingly the one-dimensional algorithm over-predicts the magnitude of the electrostatic stresses acting on the pinch region in this range of N_{Oh}. Results shown for $N_{Oh} = 1$ indicate that even at higher N_{Oh}, for which the two-dimensional algorithm predicts that the magnitude of the electrostatic stress acting at the pinch point is comparable to the capillary stress, the one-dimensional algorithm consistently overestimates $-p_E/p_C$. Again, this effect has to do with the accuracy with which the one-dimensional algorithm predicts the shape of primary drops near pinch-off. As can be seen in figure 12, the jet profile near pinch-off from a one-dimensional simulation for this set of parameters tapers more gradually toward the pinch region relative to the corresponding two-dimensional profile. This is a universal trend observed when comparing results from the two algorithms, even for uncharged jets. Because the profile of the leading edge of the primary drop increases more sharply away from the pinch region in the two-dimensional case, the shielding of the pinch region from the electric field provided by the proximity of the primary drop is more effective than what is observed in the one-dimensional case.

A number of authors have carried out local analyses of the equations of motion (Navier–Stokes, Stokes and Laplace) and have developed scaling laws to describe the local dynamics of pinch-off (Eggers 1993; Papageorgiou 1995; Keller & Miksis

1983; Day *et al.* 1998; Lister & Stone 1998), though no such scaling theories exist when electrostatic stresses are important. For uncharged jets in the inviscid limit, the dynamics of pinch-off are described by potential-flow (PF) scaling theory (Keller & Miksis 1983; Chen & Steen 1997; Day *et al.* 1998), which dictates that the radial and axial length scales in the pinch region vary as $\tau^{2/3}$ as $h_{min} \to 0$, where τ is the time remaining until breakup, $\tau = t_b - t$, and t_b is the breakup time. For uncharged Newtonian jets at low N_{Oh}, the pinch-off dynamics follow the PF scaling law until h_{min} becomes $O(N_{Oh}^2)$ (Lister & Stone 1998), at which point, viscous effects begin to become important. Beyond this point, the pinch-off dynamics are described by the inertial-viscous (IV) scaling theory (Eggers 1993), for which the local radial and axial length scales vary as τ and $\tau^{1/2}$, respectively. Notz *et al.* (2001), Chen *et al.* (2002) and Notz & Basaran (2004) have demonstrated this transition computationally using algorithms similar the two-dimensional algorithm used here.

If, as postulated above, however, an applied electric field does not influence pinch-off dynamics at low to moderate N_{Oh}, the local dynamics of the pinch region for charged, slightly viscous jets should follow the same scaling laws dictated for uncharged slightly viscous jets. For slightly viscous jets with $N_{Oh} = 0.01$, for example, the pinch-off dynamics should be governed by PF scaling theory until $h_{min} \sim 10^{-4}$, beyond which the pinch-off dynamics should follow the IV scaling law. Figure 36 shows that the thinning dynamics of both uncharged and highly charged ($N_E = 5$), slightly viscous ($N_{Oh} = 0.01$) jets match PF scaling theory, demonstrating that the application of even a strong electric field has no discernible influence on pinch-off dynamics of jets at low N_{Oh}. The results shown are from two-dimensional simulations using Mesh I with $N_{z1} = 500$. Figure 36(*a*) shows the variation of h_{min} with τ both for uncharged ($N_E = 0$) and highly charged ($N_E = 5$), slightly viscous ($N_{Oh} = 0.01$) jets. In both cases, it has been found that h_{min} varies as $\tau^{2/3}$, demonstrating that the radial length scale follows the power-law scaling predicted by the PF scaling law. Further, there is virtually no discernible difference between the h_{min} *vs.* τ curves for the uncharged jet and the highly charged jet.

For uncharged jets, because of the orders of magnitude disparity between the local length and time scales in the proximity of pinch-off and the corresponding global scales, the interface shapes in the vicinity of the pinch point must be self-similar and hence, when properly scaled, should collapse onto a single profile. As both the local axial and radial length scales vary as $\tau^{2/3}$ in the PF regime, scaling h and $z - z_{min}$ by h_{min} produces the desired collapse. Figure 36(*b*) shows a sequence of profiles with h and z scaled by h_{min} for both uncharged and highly charged ($N_E = 5$), moderately viscous jets in the vicinity of the pinch point at τ corresponding to $h_{min} = 0.016$, $h_{min} = 0.008$ and $h_{min} = 0.004$. Both the uncharged and highly charged profiles, when scaled according to PF scaling theory, demonstrate self-similarity. Further, the scaled uncharged and highly charged profiles become nearly indistinguishable as pinch-off is approached. These results strongly support the assertion that the applied electric field has no discernible influence on the local pinch-off dynamics at low N_{Oh}.

4. Conclusions

A robust and accurate three-dimensional but axisymmetric G/FEM algorithm, referred to here as the two-dimensional algorithm, has been developed in this paper to examine the dynamics of jets of perfectly conducting, incompressible Newtonian liquids that are stressed by a radial electric field. Additionally, a computationally inexpensive hybrid algorithm, referred to here as the one-dimensional algorithm,

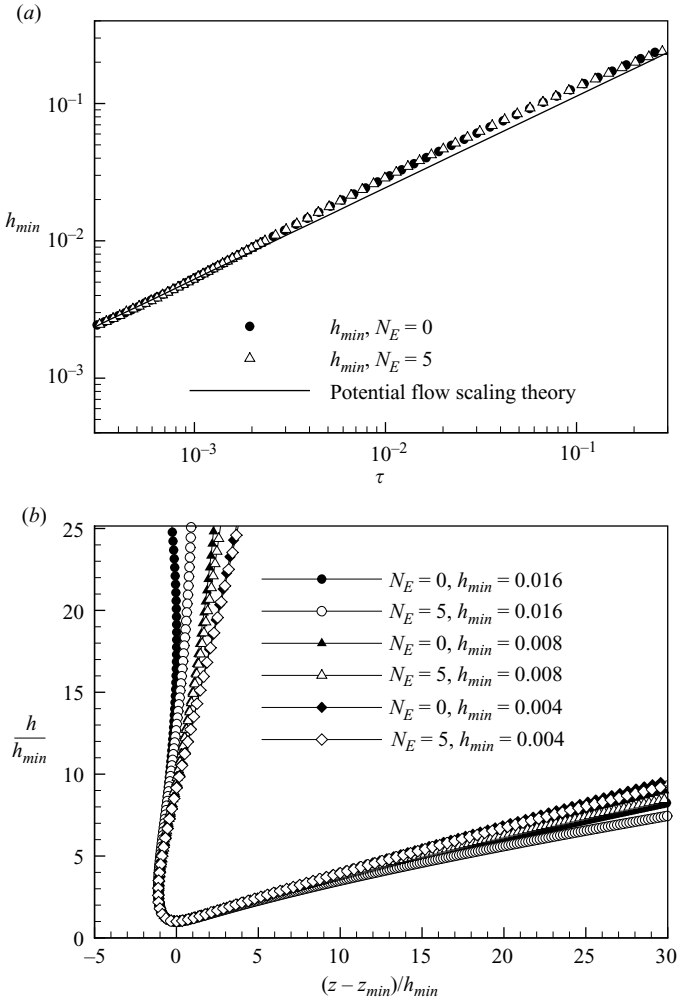

FIGURE 36. (*a*) Variation of h_{min} with τ for uncharged and highly charged ($N_E = 5$), slightly viscous jets of $N_{Oh} = 0.01$. (*b*) Self-similarity of scaled jet profiles for uncharged and highly charged ($N_E = 5$), slightly viscous jets of $N_{Oh} = 0.01$. Jet profiles in the vicinity of h_{min} from two-dimensional simulations are shown at various τ close to pinch-off for which h and $z - z_{min}$ have been scaled by h_{min}. In both (*a*) and (*b*), $k = 0.6$.

based on a slender-jet approximation of the equations governing the flow within the jet to analyse the dynamics has also been developed. Both algorithms are used to follow the jet dynamics all the way to breakup. Both algorithms are demonstrated to be in excellent agreement with linear theory at times well prior to breakup. Detailed comparisons of the predictions of the two algorithms reveal that the one-dimensional algorithm can predict accurately certain gross features of the dynamics such as breakup times and the volumes of drops formed at pinch-off.

The mechanisms responsible for satellite drop formation from the breakup of electrified jets have been examined thoroughly. In the absence of electric field, thin threads are known to pinch symmetrically in the Stokes flow limit, thereby precluding the formation of satellites. By contrast, it is shown here that in the presence of electric field, satellites form even in the Stokes flow limit. Computations reveal that the sizes

of the satellite drops formed from the breakup of electrified jets will always be larger than their counterparts formed from the breakup of uncharged jets at the same values of the Ohnesorge number and disturbance wavenumber. An equally interesting issue is the Coulombic stability of both the satellite and primary drops formed at pinch-off. It is shown in this work that satellite drops formed from viscous jets are particularly unstable, especially when jets are subjected to short-wavelength perturbations at low to moderate electric Bond numbers.

In the absence of electric field, interfaces of inviscid and low-N_{Oh} liquids are known to overturn prior to pinch-off. Here, the application of an electric field is shown to enhance overturning. This finding has a profound influence on the local dynamics of pinch-off. Occurrence of overturning results in total shielding of the pinch region from the electric field. Therefore, electrostatic stresses do not influence the local dynamics of pinch-off of filaments of liquids of low to moderate N_{Oh}. In contrast, at large N_{Oh} and in the Stokes flow limit, the electrostatic stresses acting in the pinch region of highly charged electrified jets are found to be of the same order of magnitude as capillary stresses. For a scaling theory to describe accurately the local dynamics of pinch-off at large N_{Oh} or in the Stokes flow limit, proper account must be taken of these large electrostatic stresses. However, as this work demonstrates, the local electric field acting in the pinch region depends strongly on the global shape of the jet, as the proximity of the primary drop provides partial shielding of the pinch region from the applied field even in the Stokes flow limit. It would appear, then that the possibility of a self-similar universal scaling law describing the pinch-off of electrified jets at high N_{Oh} or in the Stokes flow limit may be precluded. Development of a complete theoretical understanding of the local dynamics governing pinch-off of electrified filaments is left as an open problem of fluid mechanics.

This work was supported by the Shreve Trust Fund at Purdue University and the BES Program of US DOE.

Appendix A. The perfect conductor model and choice of parameter values

A liquid jet can be treated as a perfect conductor if the the charge relaxation time $t_e \equiv \epsilon^*/\sigma$, where σ and ε^* are, respectively, the conductivity and permittivity of the jet liquid, is much smaller than the capillary time scale $t_c \equiv \sqrt{\rho \tilde{R}_1^3/\gamma}$, namely $t_e \ll t_c$. For example, Zhang & Basaran (1996) used aqueous solutions of sodium chloride in their experimental study of dripping and jetting from a capillary in an electric field. For these solutions, the charge relaxation time ranges from $t_e \approx 10^{-4}$ s for pure water to $t_e \approx 10^{-7}$ s for 1 mM NaCl, while $t_c \approx 10^{-4}$ s for a 100 μm jet. Thus, the perfect conductor model is certainly appropriate for describing the breakup of jets of the more concentrated solutions of NaCl used in their experiments. López-Herrera & Gañan-Cálvo (2004) used mixtures of different concentrations of glycerol in tap water in their experiments on breakup of electrified jets where the jets have radii of $O(100\,\mu\text{m})$. These authors have reported that $t_e/t_c = O(10^{-4})$, thereby justifying the use of the perfect conductor model. Therefore, the conditions required for the perfect conductor model adopted in this paper to be applicable can readily be achieved in experiments. It should be noted, however, that the perfect conductor model does not apply in all cases where cone-jetting occurs. Gamero-Castaño & Hruby (2002), for example, examined experimentally the sizes of drops formed from cone-jets of tributyl phosphate solutions. For each experimental result reported in that work, when the radius of the drops formed is used as the characteristic length scale, the resulting

capillary time is smaller than the charge relaxation time. Clearly, it is inappropriate to treat the jets as perfect conductors in such situations.

The range of Ohnesorge numbers examined in this paper is determined by the desire to be comprehensive. For a 100 μm jet of NaCl solutions described above, $N_{Oh} \approx 10^{-2}$. By using solutions of glycerol–tap water, as in the experiments of López-Herrera & Gañan-Cálvo (2004), values of the Ohnesorge number as high as 10 can readily be attained.

The range of electric Bond numbers considered in this paper corresponds roughly to that examined experimentally by López-Herrera & Gañan-Cálvo (2004) for which axisymmetric breakup is observed (see, for example, figure 9 of that work, which indicates that a transition from axisymmetric breakup to asymmetric breakup occurs between $N_E \approx 3.5$ and $N_E \approx 5$ for jets of $N_{Oh} \approx 0.08$). It is only in § 3.4.5 that slightly higher values of N_E are considered. It is clearly stated in this section that results for these higher N_E are included here for the purpose of comparison with results previously reported by Setiawan & Heister (1997). The latter paper is often cited by others who benchmark their results against it. Further, it is explicitly stated in § 3.4.5 that the results for these high values of N_E are most likely unphysical and that these solutions would be unstable with respect to three-dimensional disturbances.

Appendix B. Domain tessellation and mesh refinement

B.1. *Two-dimensional algorithm*

The elliptic mesh generation algorithm used here is based on the method of Christodoulou & Scriven (1992). The weighted residuals of the equations governing the mesh are

$$R_\xi^i = \int_\Omega \left[\sqrt{\frac{z_\xi^2 + r_\xi^2}{z_\eta^2 + r_\eta^2}} + \epsilon_s \right] \nabla\xi \cdot \nabla\phi^i |J| \, \mathrm{d}\eta \, \mathrm{d}\xi - \epsilon_\xi \int_\Omega f(\xi) \ln\left(z_\xi^2 + r_\xi^2\right) \phi_\xi^i \, \mathrm{d}\eta \, \mathrm{d}\xi - M_\xi \int_{\partial\Omega} f(\xi) \ln\left(z_\xi^2 + r_\xi^2\right) \phi_\xi^i \, \mathrm{d}\xi, \quad \text{(B 1)}$$

$$R_\eta^i = \int_\Omega \left[\sqrt{\frac{z_\eta^2 + r_\eta^2}{z_\xi^2 + r_\xi^2}} + \epsilon_s \right] \nabla\eta \cdot \nabla\phi^i |J| \, \mathrm{d}\eta \, \mathrm{d}\xi - \epsilon_\eta \int_\Omega g(\eta) \ln\left(z_\eta^2 + r_\eta^2\right) \phi_\eta^i \, \mathrm{d}\eta \, \mathrm{d}\xi - M_\eta \int_{\partial\Omega} g\,(\eta) \ln\left(z_\eta^2 + r_\eta^2\right) \phi_\eta^i \, \mathrm{d}\eta, \quad \text{(B 2)}$$

where J represents the Jacobian of the transformation from the physical domain to the computational domain and $\partial\Omega$ is the boundary of the domain. Equations (B 1) and (B 2) determine a set of curves of constant ξ and η that intersect at the mesh points. The weighting parameters ϵ_s, ϵ_ξ and ϵ_η, and M_ξ and M_η control, respectively, the smoothness of the ξ and η coordinate lines, the concentration of interior mesh points, and the concentration of boundary mesh points. The functions $f(\xi)$ and $g(\eta)$ are chosen so as to concentrate (dilute) the mesh points in the ξ or η directions in regions where $f(\xi)$ or $g(\eta)$ are large (small).

For resolving the breakup of electrified jets at low to moderately high electric Bond numbers with the two-dimensional algorithm, the computational domain is divided into four regions. Hereinafter, this mesh is referred to as Mesh I. Region I corresponds to the domain of the liquid jet, Ω_1, while Regions II, III and IV correspond to the domain of the outer fluid, Ω_2. Four independent parameters are

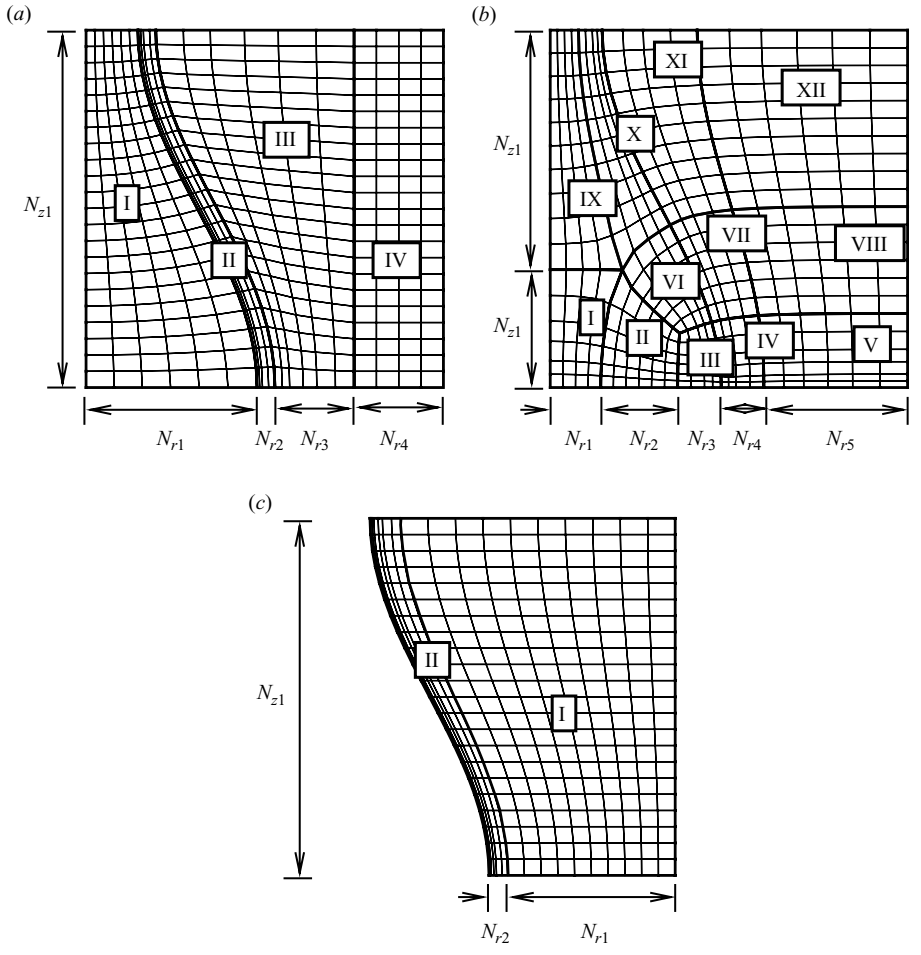

FIGURE 37. Coarse examples of sample meshes used with (*a*) the two-dimensional algorithm, Mesh I, (*b*) the two-dimensional algorithm, Mesh II, and (*c*) the one-dimensional algorithm.

required to characterize this mesh: N_{z1}, which equals the number of axial elements in Regions I–IV, and N_{r1}, N_{r2}, N_{r3} and N_{r4}, which denote the numbers of radial elements in Regions I, II, III and IV, respectively. A coarse sample mesh is shown in figure 37(*a*). The elliptic mesh algorithm described above is used in Regions I and III to determine the mesh point locations, with $f(\xi)$ and $g(\eta)$ chosen to concentrate mesh points near the free surface S_f. To increase computational efficiency, a fixed algebraic mesh is used in Region IV. An adaptive algebraic mesh algorithm is employed in Region II for the purpose of mesh point concentration. This is done in order to resolve the sharp gradients in Φ which arise in the vicinity of the slender neck region that develops as pinch-off is approached and distinguishes the present mesh generation algorithm from its predecessors (Chen *et al.* 2002; Notz & Basaran 2004). The new algorithm used to tessellate Region II first determines the direction of the η coordinate lines at the free surface S_f, which corresponds to a curve of constant ξ, in Region I at the previous time step and then constructs the η coordinate lines in Region II by moving outward from S_f along these directions. The directions are determined from the previous time step for computational efficiency. The ξ coordinate

lines are then chosen so that the mesh points in Region II are concentrated near S_f according to a desired weighting function. Typically, the width of Region II is chosen to be small ($O(0.001) - O(0.01)$) and is exaggerated for clarity in figure 37(a).

When the breakup of electrified jets at very high N_E is examined, a more complex tessellation of the computational domain is required Hereinafter, this mesh is referred to as Mesh II. This is necessitated by the extreme radial elongation of the portion of the jet that forms the primary drop which is characteristic of jet breakup at very high N_E. Figure 37(b) shows a coarse example of the mesh used in these situations. Here, the computational domain is divided into twelve regions. Regions I, II, III, VI, IX and X correspond to the domain of the liquid jet, Ω_1, while Regions IV, V, VII, VIII, XI and XII correspond to the domain of the outer fluid, Ω_2. Seven independent parameters are used to characterize this mesh: N_{z1}, the number of axial elements in Regions I, II, III, IV and V; N_{z2}, the number of axial elements in Regions IX, X, XI and XII; N_{r1}, the number of radial elements in Regions I and IX; N_{r2}, the number of radial (axial) elements in Region II (Regions VI, VII and VIII); N_{r3}, the number of radial elements in Regions III, VI and X; N_{r4}, the number of radial elements in Regions IV, VII and XI; and N_{r5}, the number of radial elements in Regions V, VIII and XII. The elliptic mesh algorithm described above is used in each of these regions. The functions $f(\xi)$ and $g(\eta)$ are chosen such that the mesh points are concentrated near S_f in Regions III, IV, VI, VII, X and XI and near $S_{1,b}$ ($S_{2,b}$) in Regions I, II and III (IV and V).

To determine the optimal mesh for a given set of dimensionless groups, the mesh parameters described above must be varied independently until the computed solutions are insensitive to further increases in each N_{zj} and N_{rj}. Measures used to determine the insensitivity of the mesh to further refinement include the time required for the jet to break, the volumes of the drops (primary and satellite) formed at pinch-off, and the surface charge on the drops (primary and satellite) formed at pinch-off. The mesh is considered to be insensitive to further refinement when an increase in any of the mesh parameters results in a change of $<0.2\%$ in each of these measures. For Mesh I, the optimal mesh parameters for meeting these criteria for $k = 0.6$ and $R_2 = 10$ are: $N_{z1} = 200$, $N_{r1} = 6$, $N_{r2} = 3$, $N_{r3} = 18$ and $N_{r4} = 5$. The optimal mesh for meeting these criteria is relatively insensitive to changes in N_{Oh} for the range of N_{Oh} examined in this work and to changes in N_E for low to moderately high N_E (i.e. $N_E \leqslant 5$). To obtain a similar degree of insensitivity to further refinement for longer waves, it is sufficient to increase N_{z1} proportionally to the increase in wavelength, λ. Likewise, for an increase in R_2, it is sufficient to increase N_{r4} so that the radial spacing of the elements in Region IV remains unchanged. Note that the boundary between Regions III and IV is typically fixed at $r = 5$ and that Region IV is not used in cases for which $R_2 \leqslant 5$. In cases for which it is desirable to resolve in fine detail the region in the immediate vicinity of the pinch point at the incipience of pinch-off, it is necessary to increase N_{z1}. Insensitivity to further mesh refinement in this case is determined by comparing the jet profiles in the immediate vicinity of the pinch point obtained using different meshes. To resolve this pinch region in detail at $h_{min} = 2 \times 10^{-3}$ for $k \geqslant 0.6$, $N_{z1} = 500$ is sufficient, and the other mesh parameters need not be increased. For longer waves, N_{z1} must also be increased proportionally to the increase in λ. If calculations are continued beyond $h_{min} = 2 \times 10^{-3}$, additional refinement is required to produce mesh independent results.

For Mesh II, the optimal mesh parameters based on the criteria described above, with $k > 1$ and $R_2 = 10$, are: $N_{z1} = 15$, $N_{z2} = 90$, $N_{r1} = 3$, $N_{r2} = 15$, $N_{r3} = 4$, $N_{r4} = 3$ and $N_{r5} = 21$. This mesh is typically used only for jets with very short wavelengths

($k > 1$) and with very high electric Bond numbers ($N_E > 5$). Increasing R_2 requires a proportional increase in N_{r5} for similar insensitivity to refinement. For low to moderate N_E and for short wavelengths, Mesh I and Mesh II yield virtually identical results using the optimal mesh parameters reported.

B.2. *One-dimensional algorithm*

In the one-dimensional algorithm, Ω_2 is divided into two regions, in which different weighting functions are used to determine the locations of the ξ-coordinate lines and, hence, the mesh points. Three independent parameters describe this mesh: N_{z1}, the number of axial elements; N_{r1}, the number of radial elements in Region I; and N_{r2}, the number of radial elements in Region II. A coarse sample mesh is shown in figure 37(c). In Region I, the weighting function used distributes the mesh points evenly along a given spine, while in Region II, which borders the free surface S_f, the weighting function used concentrates the mesh points geometrically near S_f. The fraction of each spine spanned by Region I is typically 0.9.

As with the two-dimensional algorithm, the optimal mesh is determined by systematically varying the mesh parameters. Using the measures described for the two-dimensional algorithm, the optimal values of these parameters for $k = 0.6$ and $R_2 = 10$ have been found to be: $N_{z1} = 600$, $N_{r1} = 8$ and $N_{r2} = 12$. Larger wavelengths and/or R_2 require proportional increases in N_{z1} and/or N_{r1}, along with an increase in the fraction of each spine spanned by Region I.

Appendix C. Growth rates from one- and two-dimensional simulations

As was shown experimentally by Goedde & Yuen (1970) and computationally by Ashgriz & Mashayek (1995), the appropriate growth rate for comparison with linear theory is related to the time rate of change of the amplitude $A = A(t)$, which is defined as the difference between the maximum and the minimum values of the radial coordinates of the free-surface profile. Linear theory requires a temporally constant ω with $A \propto \exp(\omega t)$, whence it follows that $\omega = \mathrm{d}\log(A)/\mathrm{d}t$ and that the breakup time $t_b = -\log(\varepsilon)/\omega$. For the systems described by the one- and two-dimensional algorithms, the instantaneous growth rate is defined similarly as $\omega(t) = \mathrm{d}\log(A)/\mathrm{d}t$. As alluded to previously, $\omega(t)$ is expected to match the linear growth rate precisely, deviating only in the initial and final stages of the simulations so that a semi-log plot of $A(t)$ with time will be linear for most of the breakup process with a slope nearly equal to the linear growth rate. The slope is obtained from a linear regression of $\ln A(t)$ *vs.* t, with the data from the initial and final stages of the simulation excluded. Figure 38(a) presents a typical example of results obtained by this approach. In this example, the two-dimensional algorithm is used to simulate the breakup of a Newtonian liquid jet in the absence of electric field effects. Here, $\omega(t)$ is essentially constant for much of the breakup process, deviating from this linear regime only in the initial and final stages of the process. The deviations at early times stem from the use of initial conditions which are inconsistent with linear stability analysis. Such deviations can be reduced by decreasing ε.

As an example, figure 38(b), which highlights the influence of electrode position on growth rates for fixed N'_E, shows that computed growth rates from two-dimensional simulations are in excellent agreement with those obtained from the dispersion relations described by (3.1) and (3.3). As noted above, in the limit as $R \to \infty (R \gg 1/k)$ with N'_E fixed, the dispersion relation used herein reduces to Saville's dispersion relation, and this trend is clearly demonstrated in Figure 38(b).

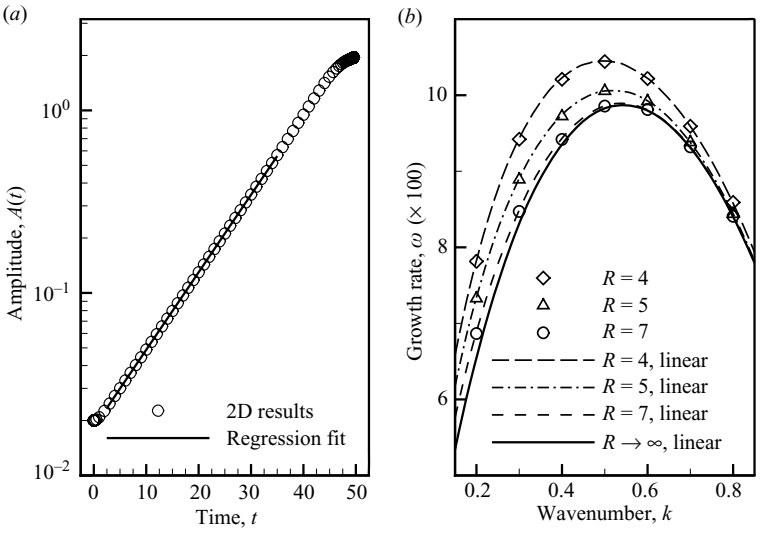

FIGURE 38. Comparison of growth rates from one- and two-dimensional computations with linear theory. Here, $N_{oh} = 1$ and $\varepsilon = 0.01$. (*a*) Procedure used to extract growth rates from one- and two-dimensional computations. The slope of the linear portion of the semi-log plot of the computed variation of the amplitude of the free surface with time provides the growth rate for comparison with linear theory. The growth rate extracted from the two-dimensional simulation, $\omega = 0.09782$, differs from the growth rate from the analytical dispersion relation, $\omega = 0.09739$, by less than 0.5%. Here, $A(t) = A_0 \exp(\omega t)$ and $k = 0.6$. (*b*) Dependence on electrode radius of the variation of growth rate with wavenumber. Growth rates from linear theory (lines) are compared with results obtained from two-dimensional simulations (symbols) over a portion of the range of unstable wavenumbers. Here, $N'_E = 2N_E/\log^2(R) = 0.7721$. Growth rates from Saville's (1971) dispersion relation ($R \to \infty$) are included for comparison.

Additional comparisons between growth rates obtained from computations and those from linear theory are provided in § 3.1.

REFERENCES

ADORNATO, P. M. & BROWN, R. A. 1983 Shape and stability of electrostatically levitated drops. *Proc. R. Soc. Lond.* A **389**, 101–117.

AMBRAVANESWARAN, B. & BASARAN, O. A. 1999 Effects of insoluble surfactants on the nonlinear deformation and breakup of stretching liquid bridges. *Phys. Fluids* **11** (5), 997–1015.

AMBRAVANESWARAN, B., WILKES, E. D. & BASARAN, O. A. 2002 Drop formation from a capillary tube: comparison of one-dimensional and two-dimensional analyses and occurrence of satellite drops. *Phys. Fluids* **14** (8), 2606–2621.

ASHGRIZ, N. & MASHAYEK, F. 1995 Temporal analysis of capillary jet breakup. *J. Fluid Mech.* **291**, 163–190.

BASARAN, O. A. 2002 Small-scale free surface flows with breakup: drop formation and emerging applications. *AIChE J.* **48**, 1842–1848.

BASARAN, O. A. & SCRIVEN, L. E. 1989 Axisymmetric shapes and stability of charged drops in an external electric field. *Phys. Fluids* A **1**, 799–809.

BASSET, A. B. 1894 Waves and jets in a viscous liquid. *Am. J. Maths* **16**, 93–110.

BRENAN, K. E., CAMPBELL, S. L. & PETZOLD, L. R. 1996 *Numerical Solution of Initial Value Problems in Differential-Algebraic Equations*. SIAM.

CHANDRASEKHAR, S. 1961 *Hydrodynamic and Hydromagnetic Stability*. Oxford University Press.

CHAUDHARY, K. C. & REDEKOPP, L. G. 1980 Non-linear capillary instability of a liquid jet.1. Theory. *J. Fluid Mech.* **96**, 257–274.

Chen, A. U., Notz, P. K. & Basaran, O. A. 2002 Computational and experimental analysis of pinch-off and scaling. *Phys. Rev. Lett.* **88** (17), 4501-1–4501-4.

Chen, Y. J. & Steen, P. H. 1997 Dynamics of inviscid capillary breakup: collapse and pinchoff of a film bridge. *J. Fluid Mech.* **341**, 245–267.

Cherney, L. T. 1999 Electrohydrodynamics of electrified liquid menisci and emitted jets. *J. Aerosol Sci.* **30**, 851–862.

Christodoulou, K. N. & Scriven, L. E. 1992 Discretization of free surface flows and other moving boundary problems. *J. Comput. Phys.* **99**, 39–55.

Cloupeau, M. & Prunet-Foch, B. 1989 Electrostatic spraying of liquids in cone-jet mode. *J. Electrostat.* **22**, 135–159.

Cloupeau, M. & Prunet-Foch, B. 1990 Electrostatic spraying of liquids–main functioning modes. *J. Electrostat.* **25**, 165–184.

Cook, K. D. 1986 Electrohydrodynamics mass-spectrometry. *Mass Spectrometry Rev.* **5**, 467–519.

Day, R. F., Hinch, E. J. & Lister, J. R. 1998 Self-similar capillary pinchoff of an inviscid fluid. *Phys. Rev. Lett.* **80** (4), 704–707.

Doshi, J. & Reneker, D. H. 1995 Electrospinning processes and applications of electrospun fibers. *J. Electrostat.* **35**, 51.

Eggers, J. 1993 Universal pinching of 3d axisymmetric free-surface flow. *Phys. Rev. Lett.* **71** (21), 3458–3460.

Eggers, J. 1997 Nonlinear dynamics and breakup of free-surface flows. *Rev. Mod. Phys.* **69**, 865–929.

Eggers, J. 2005 Drop formation–an overview. *Z. Angew. Math. Mech.* **85**, 400–410.

Eggers, J. & Dupont, T. F. 1994 Drop formation in a one-dimensional approximation of the Navier–Stokes equation. *J. Fluid Mech.* **262**, 205–221.

Fenn, J. B., Mann, M., Wong, C. K. & Whitehouse, C. M. 1990 Electrospray ionization–principles and practice. *Mass Spectrometry Rev.* **9**, 37–70.

Gamero-Castaño, M. & Hruby, V. 2002 Electric measurements of charged sprays emitted by cone jets. *J. Fluid Mech.* **459**, 245–276.

Gañan-Cálvo, A. M. 1997 On the theory of electrohydrodynamically driven capillary jets. *J. Fluid Mech.* **355**, 165–188.

Goedde, E. F. & Yuen, M. C. 1970 Experiments on liquid jet instability. *J. Fluid. Mech.* **40**, 495–511.

Gresho, P. M., Lee, R. L. & Sani, R. L. 1980 On the time-dependent solution of the incompressible Navier-Stokes equations in two and three dimensions. In *Recent Advances in Numerical Methods in Fluids* (ed. C. Taylor & K. Morgan), vol. 1, chap. 2, pp. 22–79. Pineridge.

Harris, M. T., Scott, T. C. & Byers, C. H. 1993 The synthesis of metal hydrous oxide particles by multiphase electrodispersion. *Mat. Sci. Engng* A **162**, 125–129.

Hayati, I., Bailey, A. I. & Tadros, T. F. 1987*a* Investigations into the mechanisms of electrohydrodynamic spraying of liquids 1. Effect of electric-field and the environment on pendant drops and factors affecting the formation of stable jets and atomization. *J. Colloid Interface Sci.* **117**, 205–221.

Hayati, I., Bailey, A. I. & Tadros, T. F. 1987*b* Investigations into the mechanism of electrohydrodynamic spraying of liquids 2. Mechanism of stable jet formation and electrical forces acting on a liquid cone. *J. Colloid Interface Sci.* **117**, 222–230.

Higuera, F. J. 2004 Current/flow-rate characteristic of an electrospray with a small meniscus. *J. Fluid Mech.* **513**, 239–246.

Hohman, M. M., Shin, M., Rutledge, G. & Brenner, M. P. 2001*a* Electrospinning and electrically forced jets I. Stability theory. *Phys. Fluids* **13** (8), 2201–2220.

Hohman, M. M., Shin, M., Rutledge, G. & Brenner, M. P. 2001*b* Electrospinning and electrically forced jets II. Applications. *Phys. Fluids* **13** (8), 2221–2236.

Hood, P. 1976 Frontal solution program for unsymmetric matrices. *Intl. J. Numer. Meth. Engng* **10**, 379–399.

Huebner, A. L. & Chu, H. N. 1971 Instability and breakup of charged liquid jets. *J. Fluid Mech.* **49**, 361–372.

Huyakorn, P. S., Taylor, C., Lee, R. L. & Gresho, P. M. 1978 Comparison of various mixed-interpolation finite-elements in velocity–pressure formulation of Navier–Stokes equations. *Comput. Fluids* **6**, 25–35.

Jones, A. R. & Thong, K. C. 1971 Production of charged monodisperse fuel droplets by electrical dispersion. *J. Phys.* D: *Appl. Phys.* **4**, 1159.

Keller, J. B. & Miksis, M. J. 1983 Surface tension driven flows. *SIAM J. Appl. Maths.* **43**, 268–277.

Kistler, S. F. & Scriven, L. E. 1994 The teapot effect–sheet-forming flows with deflection, wetting, and hysteresis. *J. Fluid Mech.* **263**, 19–62.

Lafrance, P. 1975 Nonlinear breakup of a laminar liquid jet. *Phys. Fluids* **18** (4), 428–432.

Lee, H. C. 1974 Drop formation in liquid jets. *IBM J. Res. Develop.* **18**, 364–369.

Lister, J. R. & Stone, H. A. 1998 Capillary breakup of a viscous thread surrounded by another viscous fluid. *Phys. Fluids* **10**, 2758–2764.

López-Herrera, J. M. & Gañan-Cálvo, A. M. 2004 A note on charged capillary jet breakup of conducting liquids: experimental validation of a viscous one-dimensional model. *J. Fluid Mech.* **501**, 303–326.

López-Herrera, J. M., Gañan-Cálvo, A. M. & Perez-Saborid, M. 1999 One-dimensional simulation of the breakup of capillary jets of conducting liquids. Application to E.H.D. spraying. *J. Aerosol Sci.* **30**, 895–912.

López-Herrera, J. M., Riesco-Chueca, P. & Gañan-Cálvo, A. M. 2005 Linear stability analysis of axisymmetric perturbations in imperfectly conducting liquid jets. *Phys. Fluids* **17** (034106).

Luskin, M. & Rannacher, R. 1982 On the smoothing property of the Galerkin method for parabolic equations. *SIAM J. Numer. Anal.* **19**, 93–113.

McGough, P. T. & Basaran, O. A. 2006 Repeated formation of fluid threads in breakup of a surfactant-covered jet. *Phys. Rev. Lett.* **96** (5), 054502-1–054502-4.

Mansour, N. N. & Lundgren, T. S. 1990 Satellite formation in capillary jet breakup. *Phys. Fluids* A **2**, 1141–1144.

Melcher, J. R. 1963 *Field Coupled Surface Waves*. MIT Press.

Melcher, J. R. & Taylor, G. I. 1969 Electrohydrodynamics: a review of the role of interfacial shear stresses. *Annu. Rev. Fluid Mech.* **1**, 111–146.

Nayfeh, A. H. 1970 Nonlinear stability of a liquid jet. *Phys. Fluids* **13** (4), 841.

Notz, P. K. & Basaran, O. A. 1999 Dynamics of drop formation in an electric field. *J. Colloid Interface Sci.* **213**, 218–237.

Notz, P. K. & Basaran, O. A. 2004 Dynamics and breakup of a contracting liquid filament. *J. Fluid Mech.* **512**, 223–256.

Notz, P. K., Chen, A. U. & Basaran, O. A. 2001 Satellite drops: unexpected dynamics and change of scaling during pinch-off. *Phys. Fluids* **13**, 549–551.

Papageorgiou, D. T. 1995 On the breakup of viscous-liquid threads. *Phys. Fluids* **7**, 1529–1544.

Plateau, J. 1863 Experimental and theoretical researches on the figures of equilibrium of a liquid mass withdrawn from the action of gravity. In *Annual Report of the Board of Regents of the Smithsonian Institution*, pp. 270–283. Washington, D.C.

Rayleigh, Lord 1879 On the instability of jets. *Proc. Lond. Math. Soc.* **10**, 4–13.

Rayleigh, Lord 1882 On the equilibrium of liquid conducting masses charged with electricity. *Phil. Mag.* **14**, 184–186.

Rayleigh, Lord 1892 On the instability of a cylinder of viscous liquid under the capillary force. *Phil. Mag.* **34**, 145–154.

Reneker, D. H., Yarin, A. L., Fong, H. & Koombhongse, S. 2000 Bending instability of electrically charged liquid jets of polymer solutions in electrospinning. *J. Appl. Phys.* **87**, 4531–4547.

Reznik, S. N., Yarin, A. L., Theron, A. & Zussman, E. 2004 Transient and steady shapes of droplets attached to a surface in a strong electric field. *J. Fluid Mech.* **516**, 349–377.

Rutland, D. F. & Jameson, G. J. 1970 Theoretical prediction of sizes of drops formed in breakup of capillary jet. *Chem. Engng Sci.* **25**, 1689.

Saville, D. A. 1971 Stability of electrically charged viscous cylinders. *Phys. Fluids* **14** (6), 1095–1099.

Saville, D. A. 1997 Electrohydrodynamics: the Taylor–Melcher leaky dielectric model. *Annu. Rev. Fluid Mech.* **29**, 27–64.

Setiawan, E. R. & Heister, S. D. 1997 Nonlinear modeling of an infinite electrified jet. *J. Electrostat.* **42**, 243–257.

Strang, G. & Fix, G. J. 1973 *An Analysis of the Finite Element Method*. Prentice–Hall.

Sweet, R. G. 1965 High frequency recording with electrostatically deflected ink jets. *Rev. Sci. Instrum.* **36**, 131–136.

Taylor, G. I. 1964 Disintegration of water drops in an electric field. *Proc. R. Soc. Lond.* A **280**, 383–397.

Taylor, G. I. 1969 Electrically driven jets. *Proc. R. Soc. Lond.* A **313**, 453–475.

Thomas, P. D. & Brown, R. A. 1987 LU decomposition of matrices with augmented dense constraints. *Intl. J. Numer. Meth. Engng* **24**, 1451–1459.

Vonnegut, B. & Neubauer, R. L. 1952 Production of monodisperse liquid particles by electrical atomization. *J. Colloid Sci.* **7**, 616–622.

Wilkes, E. D., Phillips, S. D. & Basaran, O. A. 1999 Computational and experimental analysis of dynamics of drop formation. *Phys. Fluids* **11** (12), 3577–3598.

Yarin, A. L. 1993 *Free Liquid Jets and Films: Hydrodynamics and Rheology*. Wiley.

Yarin, A. L., Koombhongse, S. & Reneker, D. H. 2001 Bending instability in electrospinning of nanofibers. *J. Appl. Phys.* **89**, 3018–3026.

Yarin, A. L., Kataphinan, W. & Reneker, D. H. 2005 Branching in electrospinning of nanofibers. *J. Appl. Phys.* **98**, 064501.

Yildirim, O. E. & Basaran, O. A. 2001 Deformation and breakup of stretching bridges of Newtonian and shear-thinning liquids: comparison of one- and two-dimensional models. *Chem. Engng Sci.* **56**, 211–233.

Yuen, M. C. 1968 Non-linear capillary instability of a liquid jet. *J. Fluid. Mech.* **33**, 151–163.

Zeleny, J. 1917 Instability of electrified liquid surfaces. *Phys. Rev.* **10**, 1–6.

Zhang, X. G. & Basaran, O. A. 1996 Dynamics of drop formation from a capillary in the presence of an electric field. *J. Fluid. Mech.* **326**, 239–263.

Zhang, X., Padgett, R. S. & Basaran, O. A. 1996 Nonlinear deformation and breakup of stretching liquid bridges. *J. Fluid. Mech.* **329**, 207–245.